6-25-2011

The 2009 Samoa and 2010 Chile Tsunamis as Observed in the Ionosphere using GPS Total Electron Content

David A. Galvan
Jet Propulsion Laboratory, California Institute of Technology

Attila Komjathy
Jet Propulsion Laboratory, California Institute of Technology

Michael P. Hickey Ph.D.
Embry-Riddle Aeronautical University, hicke0b5@erau.edu

Anthony J. Mannucci
Jet Propulsion Laboratory, California institute of Technology

Scholarly Commons Citation

Galvan, D. A., A. Komjathy, M. P. Hickey, and A. J. Mannucci (2011), The 2009 Samoa and 2010 Chile tsunamis as observed in the ionosphere using GPS total electron content, J. Geophys. Res., 116, A06318, doi: https://doi.org/10.1029/2010JA016204

The 2009 Samoa and 2010 Chile tsunamis as observed in the ionosphere using GPS total electron content

David A. Galvan,[1] Attila Komjathy,[1] Michael P. Hickey,[2] and Anthony J. Mannucci[1]

Received 12 October 2010; revised 15 March 2011; accepted 23 March 2011; published 25 June 2011.

[1] Ground-based Global Positioning System (GPS) measurements of ionospheric total electron content (TEC) show variations consistent with atmospheric internal gravity waves caused by ocean tsunamis following two recent seismic events: the Samoa earthquake of 29 September 2009 and the Chile earthquake of 27 February 2010. Both earthquakes produced ocean tsunamis that were destructive to coastal communities near the epicenters, and both were observed in tidal gauge and buoy measurements throughout the Pacific Ocean. We observe fluctuations in TEC correlated in time, space, and wave properties with these tsunamis using the Jet Propulsion Laboratory's Global Ionospheric Mapping software. These TEC measurements were band-pass filtered to remove ionospheric TEC variations with wavelengths and periods outside the typical range for tsunamis. Observable variations in TEC appear correlated with the tsunamis in some locations (Hawaii and Japan), but not in others (Southern California or near the epicenters). Where variations are observed, the typical amplitude tends to be ~0.1–0.2 TEC units for these events, on the order of ~1% of the background TEC value. These observations are compared to estimates of expected tsunami-driven TEC variations produced by Embry Riddle Aeronautical University's Spectral Full Wave Model, an atmosphere-ionosphere coupled model, and are found to be in good agreement. Significant TEC variations are not always seen when a tsunami is present, but in these two events the regions where a strong ocean tsunami was observed coincided with clear TEC observations, while a lack of clear TEC observations coincided with smaller sea surface height amplitudes. There exists the potential to apply these detection techniques to real-time GPS TEC data, providing estimates of tsunami speed and amplitude that may be useful for early warning systems.

Citation: Galvan, D. A., A. Komjathy, M. P. Hickey, and A. J. Mannucci (2011), The 2009 Samoa and 2010 Chile tsunamis as observed in the ionosphere using GPS total electron content, *J. Geophys. Res.*, *116*, A06318, doi:10.1029/2010JA016204.

1. Introduction

[2] Tsunamis have been a significant threat to humans living in coastal regions throughout recorded history. The Sumatra tsunami of 2004 took the largest toll of human life on record, with approximately 228,000 casualties attributed to the waves [e.g., *Cosgrave*, 2007]. Recent events have been sobering reminders of the hazard: the tsunami of 29 September 2009 caused an estimated 192 deaths on the islands of Samoa, American Samoa, and Apia, and estimates for casualties from the Chilean tsunami of 27 February 2010 have ranged from 124 to 231 [e.g., *Tang et al.*, 2010; NOAA National Geophysical Data Center, http://www.ngdc.noaa.gov/hazard/hazards.shtml]. Both tsunamis also had a major impact on public consciousness far afield from the epicenters, as the time period between the earthquakes and the arrival of the tsunamis at Hawaii and other communities on the Pacific Rim, such as Japan and the U.S. West Coast, caused much anxiety and coverage on major news networks. This highlights the need for effective and reliable modeling and observational systems that can provide estimates of tsunami properties before the tsunami itself arrives at a given shore. Recent modeling results have demonstrated that the ionospheric signature of an ocean tsunami can potentially be detected as traveling ionospheric disturbances (TIDs) produced by internal gravity waves propagating obliquely upward in the atmosphere [e.g., *Occhipinti et al.*, 2006, 2008; *Hickey et al.*, 2009; *Mai and Kiang*, 2009]. These tsunami-driven TIDs have been demonstrated to be present in ionospheric total electron content (TEC) measurements using ground-based GPS radio signals [e.g., *Artru et al.*, 2005; *Rolland et al.*, 2010] and satellite-based altimeter radar [*Occhipinti et al.*, 2006].

[3] *Daniels* [1952] first postulated that ocean surface waves could produce pressure waves in the atmosphere powerful enough to perturb ionospheric electron density by ~1% of the background density value. *Hines* [1960, 1972]

[1]Ionospheric and Atmospheric Remote Sensing Group, Jet Propulsion Laboratory, California Institute of Technology, Pasadena, California, USA.
[2]Department of Physical Sciences, Embry Riddle Aeronautical University, Daytona Beach, Florida, USA.

0148-0227/11/2010JA016204

[also *Hines et al*., 1974] later developed a theory of atmospheric gravity waves, and mentioned the possibility that tsunamis, in addition to other terrestrial and atmospheric events like earthquakes and tropospheric storms, might generate internal gravity waves that could propagate to altitudes greater than 70 km. *Peltier and Hines* [1976] then demonstrated mathematically that the variations in ionospheric electron densities caused by these tsunami-driven internal gravity waves should be detectable in ionosonde measurements.

[4] The only gravity waves capable of propagating to ionospheric heights are those that oscillate below the Brunt-Väisälä frequency (ω_B), the natural buoyancy frequency at which a parcel of air will oscillate when displaced from its equilibrium position [e.g., *Kelley*, 2009]. Essentially, a parcel of air that is displaced upward in the atmosphere will find itself surrounded by air that is less dense than itself, and will fall back downward until it is surrounded by air that is more dense, at which point it will be buoyed upward again, oscillating about the equilibrium height at a frequency of $\omega_B = \sqrt{(g/\theta)(d\theta/dz)}$, where g is the acceleration due to gravity, θ is the potential temperature, and z is the altitude. In the Earth's atmosphere, ω_B ranges from 3.3 to 1.1 mHz depending on altitude, corresponding to a buoyancy period ~5 min at sea level, and ~15 min at 400 km altitude, near the *F* region peak of the ionosphere [*Yeh and Liu*, 1974]. A wave perturbation at the sea surface that takes longer to oscillate than the atmosphere would naturally respond, under the restoring force of buoyancy, will successfully propagate to the upper atmosphere. If the sea surface perturbation oscillates faster than the atmosphere can respond, the wave will be evanescent in the atmosphere. Tsunamis can have periods ranging from 5 min up to an hour, but the typical deep ocean period is 10–30 min. Thus a tsunami may induce an internal gravity wave that reaches the ionosphere even though the tsunami amplitude in the deep ocean is only a few centimeters. Conversely, the typical background noise of ~1 m amplitude ocean surface waves, with periods of several to tens of seconds, produce only evanescent waves in the atmosphere, with amplitudes decreasing exponentially with altitude [e.g., *Hines*, 1972].

[5] There have been several studies observing variations in ionospheric electron density associated with ocean tsunamis. These observations have typically been made using line-of-sight integrated electron density, or total electron content (TEC), measurements available from satellite-carried nadir-looking radar altimeters (e.g., on the TOPEX/Poseidon and Jason satellites), or time delay measurements of radio signals sent from GPS satellites to ground-based receivers. *Artru et al.* [2005] showed variations in TEC as observed by over 1000 receivers in the Japanese GEONET network coincident with the arrival at Japan of a tsunami generated by an earthquake in Chile in 2001. *Occhipinti et al.* [2006] and *Mai and Kiang* [2009] showed perturbations in the TEC data derived from the Jason-1 radar altimeter after the 2004 Sumatra tsunami. *Lee et al.* [2008] observed a periodic variation in lower *F* region reflection points from the incoherent scatter radar (ISR) at Arecibo, as well as periodic variations in TEC observed by several GPS receivers throughout the Caribbean, after the Sumatra tsunami of December 2004. *Rolland et al.* [2010] showed observations of tsunami-driven TIDs observed at the Hawaiian Islands during three tsunamis that passed the islands in 2006, 2009, and 2010. Such observations have demonstrated that the ionospheric signature of ocean tsunamis can indeed be remotely observed, but subsequent efforts, (including those presented in this paper) have found that detection is not always consistent from one location to the next, or even among different ionospheric pierce points within the same region. Furthermore, there are other sources for TIDs not associated with tsunamis, such as intense or large-scale tropospheric weather [*Hung et al.*, 1978, *Kelley* 1997; *Xiao et al.*, 2007], geomagnetic and auroral activity [*Richmond and Matsushita*, 1975; *Nicolls et al.*, 2004], earthquakes [*Calais and Minster*, 1995; *Artru et al.*, 2001; *Kelley et al.*, 1985], and even unknown mechanisms [e.g., *Tsugawa et al.*, 2007]. The existence of non-tsunami-driven TIDs can make detection and confirmation of tsunami association more challenging [e.g., *Artru et al.*, 2005]. In this study, we distinguish ionospheric signatures of tsunami-driven TIDs by verifying that the horizontal speed and direction of the TID match that of the ocean tsunami.

[6] In addition to observations, progress has been made in the theoretical modeling of the interaction between the ocean surface, atmosphere, and ionosphere. *Occhipinti et al.* [2006] demonstrated a three-dimensional model predicting the variation in TEC that should be observed from a given ocean tsunami amplitude and period. *Occhipinti et al.* [2008] then showed that the neutral plasma coupling involved in transferring the wave energy from the atmosphere to the ionosphere varies with the orientation of the Earth's magnetic field, leading to more efficient coupling at lower rather than higher geomagnetic latitudes. *Hickey et al.* [2009] improved on the gravity wave modeling by including the effects of wave damping via thermal conduction, ion drag, and molecular viscosity, as well as the filtering effects of background atmospheric winds. These recent modeling results have shown, for instance, that strong zonal winds in the low-latitude upper atmosphere may make the variation in TEC produced by zonal (east–west) propagating tsunamis far lower in magnitude than variations produced by meridianol (north–south) propagating tsunamis. Such geophysical subtleties affecting the ability of tsunami-driven internal gravity waves to perturb the ionosphere create additional challenges in developing a routine method of detection via GPS TEC. Still, most recent models suggest that tsunami-driven internal gravity wave should be detectable in ionospheric TEC under certain circumstances.

[7] Using Jet Propulsion Laboratory's (JPL's) Global Ionospheric Mapping (GIM) software to remove hardware biases and extract TEC measurements from GPS receivers, we have analyzed GPS TEC data from two significant recent tsunami events in an effort to determine the consistency and nature of TEC variations associated with tsunamis. We use these historical observations as test cases to evaluate whether a real-time ground-based TEC monitoring system would have been a viable contribution to the tsunami warning system for these events. We compare our observations with estimates of predicted TEC variation magnitude from the *Hickey et al.* [2009] model for ocean-atmosphere-ionosphere coupling. In this paper, we discuss observation and model

results from the Samoa tsunami of September 2009 and the Chile tsunami of February 2010.

2. Methodology

2.1. Networks of GPS Receivers

[8] Dual-frequency GPS receivers are capable of producing the time delay and phase advance observables that can be processed to generate TEC measurements [e.g., *Langley*, 1996]. Such TEC measurements have been used to study ionospheric electron density and its response to atmospheric and space phenomena for many years [e.g., *Hajj et al.*, 1994; *Basu et al.*, 1999; *Yizengaw et al.*, 2005; *Bust and Mitchell*, 2008; *Skone* 2009]. There are several major networks of ground-based GPS receivers that can be used to produce TEC observations. The International GPS Service (IGS) network, for example, is a global network of over 350 continuously operating dual-frequency GPS stations. This type of network provides widespread but sparse coverage; useful because, no matter where a tsunami occurs, there will likely be a GPS receiver in the vicinity that may be used to look for TEC variations. There are also major regional networks, such as Japan's GEONET network of over 1200 GPS stations (http://terras.gsi.go.jp/gps/geonet_top.html), and Southern California's Plate Boundary Observatory (PBO) network of over 875 stations (http://pboweb.unavco.org/), which provide highly localized but very dense coverage. These regional networks allow for corroboration of observations via many GPS TEC observations in a particular region. We utilize all GPS stations available in a particular region of interest for our studies, sometimes using stations from multiple overlapping networks.

2.2. GIM Processing

[9] For these studies, we use the Global Ionospheric Mapping (GIM) software suite [e.g., *Mannucci et al.*, 1998; *Komjathy et al.*, 2005] to process the Receiver Independent Exchange format (RINEX) files from networks of GPS receivers in order to produce TEC values between the ground receivers and GPS satellites. GIM was developed at JPL to compute high-precision slant ionospheric delay measurements by estimating and subsequently subtracting the satellite and receiver differential biases from the ionospheric observables. Overall accuracy for absolute TEC values is at the 1–2 TECU level (1 TECU = 10^{16} el/m^2). However, for our study we are interested in monitoring small-scale variations in ionospheric electron density, hence our data set consists of changes in TEC, rather than absolute TEC values. The precision uncertainty for TEC measurements using GIM processing is approximately 0.01–0.1 TECU [e.g., *Mannucci et al.*, 1998, 2004].

2.3. Slant TEC Analysis

[10] After selecting the stations of interest based on the geographic domain of a given tsunami, we process the GPS RINEX files using the GIM software. We then produce slant-TEC time series for the stations of interest in the time period when the first wavefront of the tsunami should be moving through the vicinity of the receivers. Our current technique is a method for analyzing historical tsunami events to determine whether these tsunamis produced a detectable variation in ionospheric electron density. In the future, we hope to develop algorithms that will begin monitoring particular real-time GPS receiver observations in regions based on the epicenter location of the seismic source of the tsunami.

[11] Ocean tsunamis tend to have wave periods ranging between 5 min and 1 h, depending on the ocean depth, with typical deep ocean periods of 10–30 min, wavelengths ~400 km, and speeds of ~200 m/s [e.g., *Peltier and Hines*, 1976]. In order to remove longer period variations in TEC time series (such as diurnal variations and multiple hour trends due to changing elevation angle of the receiver-satellite line of sight), we employ two methods, using the results of each method as a check against the other.

[12] First, we fit a higher-order polynomial to the TEC time series, and subtract the observed TEC values from the polynomial fit, with the residuals representing the variation in TEC due to a TID perturbation. The polynomial used to fit the time series needs to be of sufficiently high order to capture the general trend of the time series for that arc, but not so high that it introduces additional variations in the residuals due to the enforced higher order. After applying polynomial fits for several cases, we found that tenth-order was typically adequate to provide a reasonable fit to the long-term trends of the TEC measurements. In addition, since we were applying this fit-and-subtract procedure to compute residuals for thousands of time series at a time (over a thousand receivers in the case of Japan, each with up to 12 connections with GPS satellites at a given time), we decided to use the same order polynomial for all cases for ease of automation. Hence we settled on a standard tenth-order polynomial fit in our analysis codes.

[13] Second, we use a zero-phase bidirectional band-pass filter with a passband of 0.5 to 5 mHz (corresponding to wave periods of 2000 to 200 s; 33.3 min to 3.3 min) to extract variations in TEC with periods similar to that of the ocean tsunami itself.

[14] Figure 1 shows an example of these analysis techniques applied to the TEC time series from the American Samoa, Pago Pago (ASPA) GPS receiver in the hours immediately following the earthquake on 29 September 2009. Figure 1 (top) displays the absolute slant TEC (STEC) values observed in the line of sight between the ASPA receiver and the SVN 50 GPS satellite, with a tenth-order polynomial curve fit to the measurements. Figure 1 (middle) shows the residual differences between the polynomial fit and the actual observations. Figure 1 (bottom) indicates the variations in the absolute TEC after running the data through a band-pass filter. By performing these dual analyses on the GIM-processed STEC data using all GPS receivers available, we are able to more effectively search for variations in TEC that may be associated with tsunamis. Significant variations in TEC are clearly visible in Figures 1 (top), 1 (middle), and 1 (bottom), ranging from ~18:00 to 18:30 UT. The perturbation to background TEC is quite distinct, and is visible before the tsunami itself arrives at Pago Pago. However, in order to determine whether the TEC perturbation is caused by a tsunami, the earthquake itself, or some other phenomenon, we must analyze the data further to determine the horizontal speed of the traveling ionospheric disturbance. This analysis requires an understanding of the phenomenology behind atmospheric wave propagation.

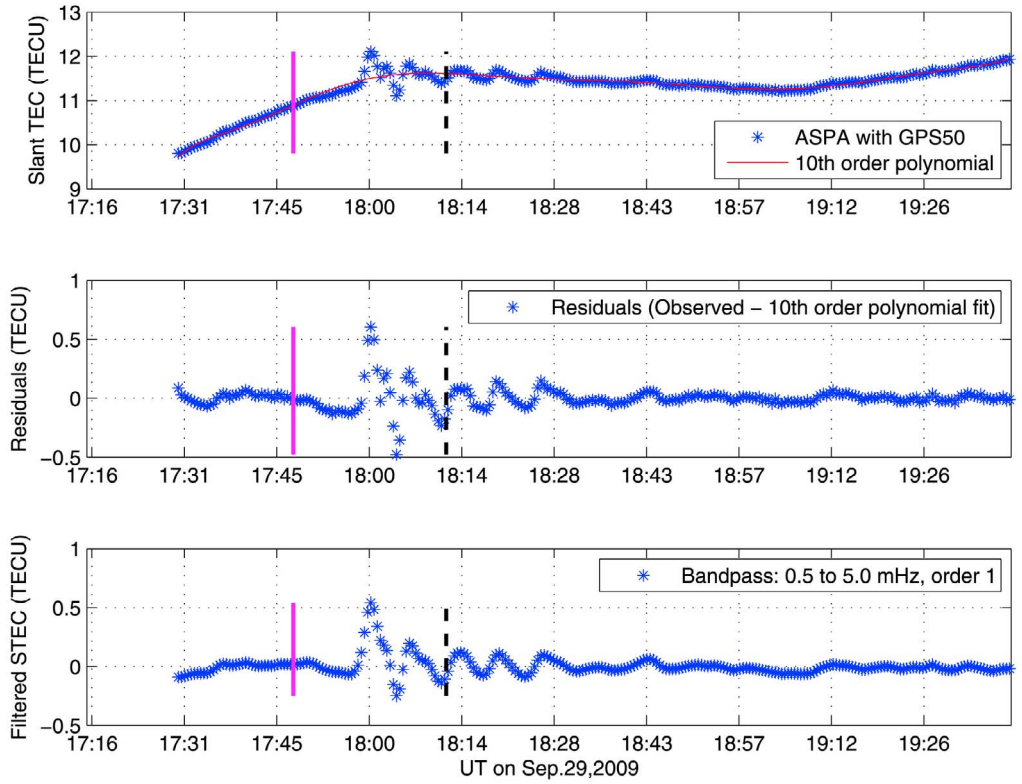

Figure 1. (top) Absolute slant TEC (STEC) versus UT time in hh:mm, (middle) residuals from a tenth-order polynomial fit, and (bottom) band-pass-filtered TEC for the Pago Pago (ASPA) GPS station and the SVN 50 satellite. The two vertical lines in each plot show the time of the earthquake (magenta solid) and the time of tsunami arrival (black dashed) at the Pago Pago tidal gauge.

2.4. Atmospheric Wave Propagation

[15] An ocean tsunami generates a fast gravity wave that propagates obliquely in the atmosphere, with both horizontal and vertical propagation velocity components. As it propagates to higher altitudes, the gravity wave's amplitude increases due to the exponential falloff of atmospheric density with increasing height. This is due to the fact that the same amount of wave energy must be carried by fewer particles, and hence the buoyancy oscillations increase in amplitude at lower atmospheric number densities. (This is partially analogous to the phenomenon of ocean waves increasing in sea surface height as they approach shore: in shallower waters, there are fewer molecules in the water column to carry the same amount of wave energy, and hence the fewer water molecules oscillate with larger amplitudes [e.g., *Hines* 1972].) Because the fast atmospheric gravity waves do not strongly attenuate until they reach the more viscous middle thermosphere, the wave amplitude continues to grow as the wave propagates upward through the ionosphere. This results in waves with much larger amplitudes in the *F* region (150–500 km altitude) than in the *E* region (90–150 km altitude) [*Hickey et al.*, 2009; *Kelley* 2009]. Also, the *F* region, which peaks in electron density between 300 and 400 km altitude (depending on local time and latitude), contains the bulk of the free electrons in the ionosphere, and therefore makes the largest contribution to measurements of ionospheric TEC. Theoretically, a sufficiently powerful gravity wave could perturb the *E* region enough to be detectable in TEC, but that perturbation would be quite small compared to the *F* region perturbation that would occur later. Hence, in our analysis we assume that any tsunami-driven atmospheric wave that could be visible as a variation in TEC would need to propagate from the ocean surface up to 400 km altitude before we could observe significant perturbations in TEC.

[16] Different types of atmospheric waves have different propagation velocities. A typical acoustic wave, often generated by earthquakes, can propagate through the atmosphere at the sound speed, which varies from several hundred m/s near sea level to ~1 km/s at 400 km altitude [e.g., *Artru et al.*, 2005]. It would take approximately 10 to 15 min for such a wave to affect the *F* region, and thus TEC observations. The initial seismic source at the epicenter can generate an acoustic wave that propagates isotropically in the atmosphere, hence both vertical and horizontal propagation speeds would be the same (the sound speed of the atmosphere). By the time the wave reaches the *F* region, the horizontal velocity of the perturbation in that region would be ~1 km/s. However, earthquakes also generate Rayleigh waves: transverse solid Earth waves that propagate along the surface with a horizontal velocity of about 3.4 km/s. These solid Earth waves, too, produce acoustic waves in the overlying atmosphere, and these acoustic waves propagate upward at the atmospheric sound speed (~300–1000 m/s depending on alti-

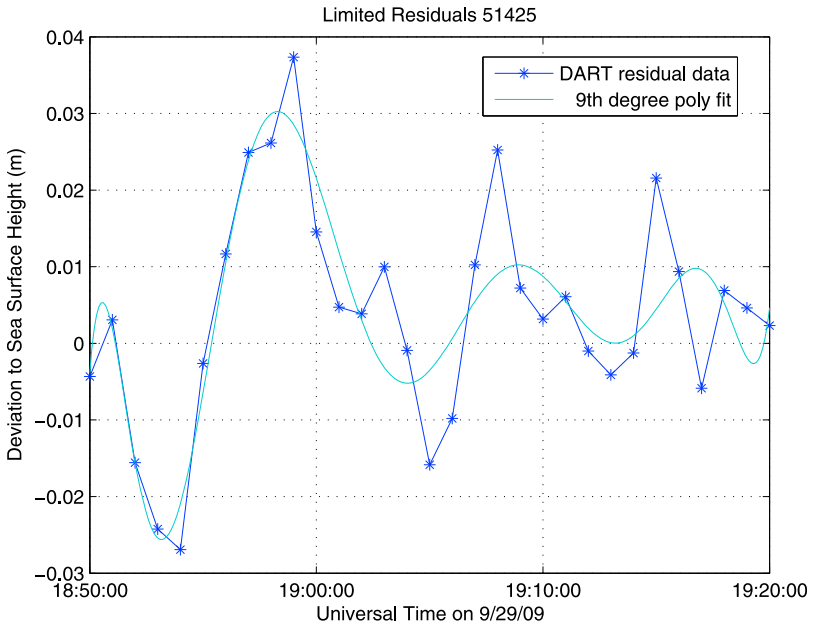

Figure 2. Variations of water column height in meters at the DART buoy 51425, located at 9.49°S, 176.25°W, northwest of American Samoa.

tude). As the Rayleigh wave moves horizontally along the Earth's crust, new atmospheric acoustic waves are generated, such that the corresponding variation in electron density in the ionosphere would appear to be moving horizontally at 3.4 km/s, following the solid Earth wave [e.g., *Artru et al.*, 2001; *Hines*, 1972]. Such earthquake-generated waves have been detected in ionospheric TEC in the past [e.g., *Calais and Minster*, 1995; *Kelley et al.*, 1985]. Earthquake-generated ionospheric disturbances must be taken into account because they could be mistaken for tsunami-driven signals but would exist regardless of whether a tsunami was generated, since not all submarine earthquakes produce tsunamis.

[17] While acoustic waves may be considered sound waves resulting from longitudinal compression in the direction of propagation, internal gravity waves are buoyancy waves resulting from vertical transverse oscillations of parcels of air caused by a slow rise and fall of the Earth's surface; in this case the ocean. With vertical propagation velocities on the order of 40–50 m/s [*Artru et al.*, 2005; *Peltier and Hines* 1976], these waves are expected to reach the *F* region in over 2 h. The horizontal velocity of observed perturbations to ionospheric TEC will match the horizontal velocity of the tsunami itself ~200 m/s. Thus, one way to distinguish signals associated with a tsunami is to search for coherent TEC variations that are propagating at ~200 m/s in an outward direction from the tsunami's source. We employed this method of finding a TEC variation of the appropriate amplitude, and then plotting the TEC values as a function of distance and time to determine if the variation is aligned with a gravity wave horizontal velocity.

2.5. Comparison With Model Results and Buoy Observations

[18] We use the *Hickey et al.* [2009] spectral full wave model (SFWM) to produce an estimate of the expected perturbation to ionospheric TEC resulting from the known ocean tsunami amplitude, period, and azimuthal direction. The SFWM numerically simulates the upward propagation of a spectrum of gravity waves in the atmosphere, and the interaction of those gravity waves with the ionosphere. The model assumes a nonisothermal atmosphere, and takes into account such subtleties as eddy and molecular diffusion of heat and momentum, as well as ion drag, Coriolis force, and the altitude variation of mean winds in the atmosphere.

[19] To produce the initial perturbation of the lower boundary of the modeled atmosphere, we use sea surface height amplitudes associated with the ocean tsunami at a given location. The sea surface height is obtained from one of two sources: the modeled height estimated by the Method of Splitting Tsunami (MOST) model produced by the NOAA Center for Tsunami Research [e.g., *Titov et al.*, 2005; *Titov and Gonzalez*, 1997; *Titov and Synolakis*, 1997], or the measurements made by various tidal gauges and ocean buoys around the world, such as the Deep-ocean Assessment and Reporting of Tsunamis (DART) buoy system throughout the Pacific Ocean [e.g., *Meinig et al.*, 2005]. (DART buoy system information is available at http://nctr.pmel.noaa.gov/Dart/dart_home.html.) This sea surface tsunami waveform (whether it is observed in buoy data or a result of the MOST model) is used as an input for the *Hickey et al.* [2009] model, which then determines the expected variation in ionospheric TEC due to the ocean surface perturbation.

3. Results

3.1. Samoa Tsunami of 29 September 2009

[20] At 17:48:11 UT on 29 September 2009, a magnitude 8.1 earthquake struck at 15.5 south latitude, 172.0 west longitude, 195 km south of Apia, Samoa. The earthquake produced a tsunami that arrived at the city of Pago Pago on

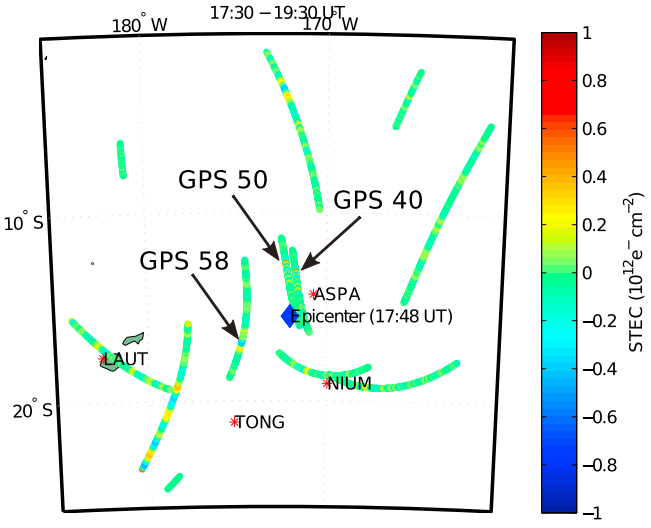

Figure 3. Time-convolved time series showing band-pass-filtered STEC at ionospheric pierce points from the ASPA station for the 2 h following the earthquake that caused the Samoa tsunami. Wave-like variations are visible in the time series from GPS satellites, 40, 50, and 58.

American Samoa at 18:12 UT, according to nearshore tidal gauges, causing significant damage. Figure 1 shows STEC measurements from the GPS receiver at Pago Pago (ASPA) for 2 h after the earthquake took place. The first (magenta) vertical line in Figure 1 shows the time at which the earthquake occurred (17:48 UT), and the second (black) vertical line shows the time at which the tsunami was observed in the Pago Pago tidal gauge (18:12 UT). Both the residuals (Figure 1 (middle) the difference between the observed STEC and a tenth-order polynomial fit) and the band-pass-filtered STEC (Figure 1, bottom) show significant variations with amplitudes up to ~0.5 TECU at first and then around 0.1– 0.2 TECU following the initial signal. These take place as early as 10 min after the earthquake occurs, but also 10 min before the ocean tsunami was observed at the Pago Pago tidal gauge. Wave periods observed in the TEC measurements are ~10 min. Figure 2 indicates the observed deviations to sea surface height at DART buoy 51425, located several hundred kilometers northwest of American Samoa. The DART buoy observed the tsunami about 40 min after the wave hit American Samoa, due to the buoy's greater distance from the epicenter. Note, however, that the tsunami wave period in the deep ocean where the DART buoy is located was approximately 10 min, similar to what was observed in the TEC variations shown in Figure 1. Similar observations are visible in TEC data from other GPS satellites in view of the ASPA site.

[21] Figure 3 displays a map of the area of the South Pacific surrounding American Samoa, showing the epicenter of the earthquake as well as the location of the ASPA and other GPS ground stations for reference. The colored tracks denote the locations of the ionospheric pierce points; the points at which the line of sight between the ASPA receiver (only) and various GPS satellites penetrate the *F* region at the ionospheric shell height (selected to be 400 km in our case), where the variation in TEC is expected to be the most significant. The ionospheric pierce points appear as long tracks because Figure 3 displays 2 h worth of data, with pierce points moving along with the GPS satellites' lines of sight. The color itself represents the variation in TEC obtained by running the STEC time series through a band-pass filter, as in Figure 1 (bottom). In addition to the variations in the connection to SVN 50 (as was shown in Figure 1), there are similar wave-like variations in the TEC observations from SVN 40 and SVN 58.

[22] At first glance these observations might seem to suggest that a tsunami-driven TID is visible in the ASPA STEC data. However, if the observed variations are caused by an internal gravity wave from the tsunami, the gravity wave must have propagated from the surface of the ocean to the *F* region of the ionosphere within approximately 15 min. Theoretical vertical propagation speeds of internal gravity waves are ~50 m/s [e.g., *Artru et al.*, 2005, *Peltier and Hines*, 1976], which would result in a 2.2 h propagation time from the surface of the ocean to the *F* region peak at 400 km altitude.

[23] The vertical propagation velocity of an atmospheric gravity wave was discussed in detail by *Hines* [1960] and was further summarized by *Peltier and Hines* [1976]. It can be described as the vertical component of the group velocity, defined as

$$v_z = \omega k_z \left[\omega^2/c^2 - \omega_B^2 k_x^2/\omega^2\right]^{-1} \quad (1)$$

where ω is the frequency of the atmospheric gravity wave, k_x and k_z are the horizontal and vertical wave numbers, respectively, c is the speed of sound, and ω_B is the Brunt-Väisälä frequency. From equation (1), we can obtain a

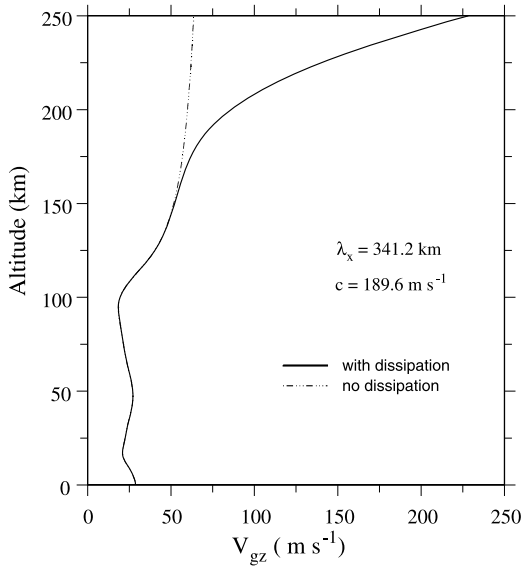

Figure 4. Vertical group speed calculated for the 2009 Samoa tsunami, as observed near Hawaii (average speed c = 189.6 m/s, T = 30 min, λ_x = 341.2 km). Calculated using the dissipationless dispersion equation of *Hines* [1960] (dashed curve) and dispersion equation of *Hickey and Cole* [1987] (solid curve), which includes the effects of dissipation. Dissipation removes slower waves from a wave packet, which leads to an increase in the group speed.

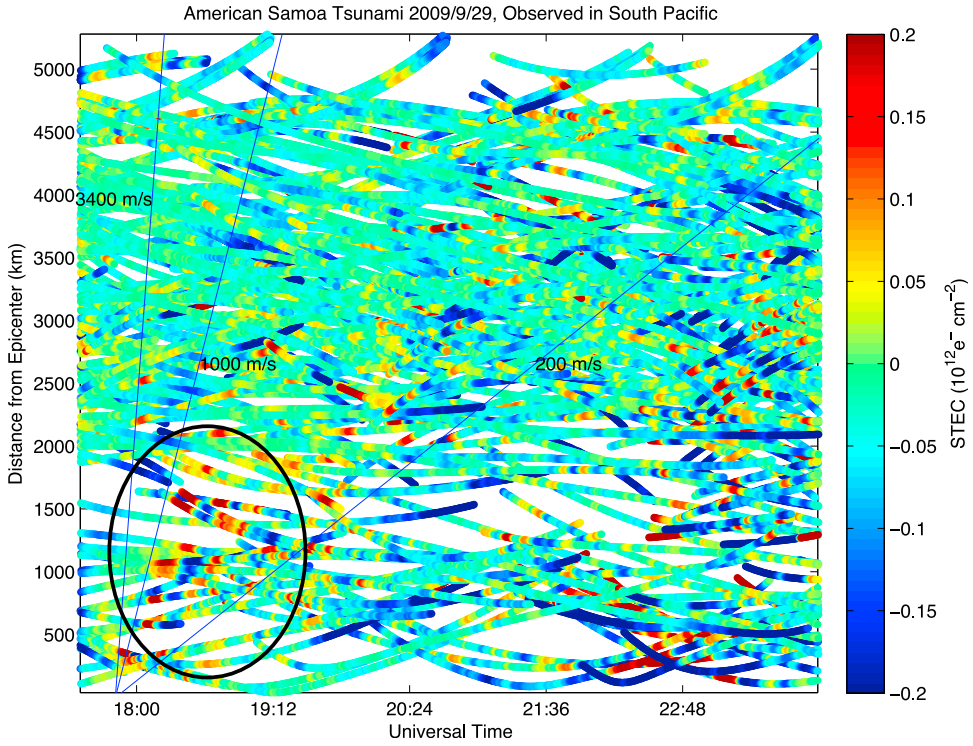

Figure 5. Variations in STEC plotted as a function of distance from the Samoa earthquake epicenter and UT. Overplotted lines show alignment of waves at different horizontal velocities: 3400 m/s for Rayleigh waves, 1000 m/s for acoustic waves, and 200 m/s for tsunami-driven internal gravity waves. Oval highlights TID disturbance aligned roughly parallel to the acoustic wave horizontal speed.

profile of vertical group velocity versus altitude by varying the temperature (and hence the sound speed value) as a function of altitude.

[24] Figure 4 shows a profile of vertical propagation velocities for a tsunami-driven atmospheric gravity wave as a function of altitude. The dashed curve uses the *Hines* [1960] dispersion relation to calculate k_z as cited above and as summarized by *Peltier and Hines* [1976], which excludes dissipation. The solid curve uses the dispersion relation of *Hickey and Cole* [1987] which uses an eighth-order dispersion equation in k_z to calculate $\partial\omega/\partial k_z$. That dispersion equation includes the effects of dissipation due to thermal conduction and viscosity. It also uses the shallow atmosphere approximation to include the effects of the Coriolis force. For tsunami wave periods (~30 min or less) the error introduced by the approximation is insignificant (see *Hickey and Cole* [1987] for a thorough explanation of this, especially their Figure 7). Both the Hines and the Hickey and Cole dispersion equations are based on an isothermal atmosphere, though group velocity values are calculated using local temperature and sound speed values at each height, thus showing the variation of group velocity with altitude. For the wave-specific parameters, we use the speed, wavelength, and period of the Samoa tsunami as observed near the Hawaiian Islands: average speed 189.5 m/s, period 30 min, wavelength 341.1 km. The average speed was calculated based on the arrival time of the tsunami at the tidal gauge in Hilo on the Big Island, the period was extracted from the MOST model of the tsunami in deep water off the Hawaiian Islands, and the wavelength was calculated from the period and average speed.

[25] At altitudes greater than 150 km, dissipation preferentially removes the slower waves (of large k_z) from the spectrum, leading to an increase in v_z because the faster waves remain. The time for a gravity wave to reach 200 km given the vertical group velocities shown in Figure 4 is 1.6 h for *Hickey and Cole* [1987] and 1.8 h for *Hines* [1960]. When integrating these curves to determine the arrival time of the gravity wave in the *F* region, we find that the longest estimate comes from the original *Hines* [1960] description, which does not include dissipation and thus predicts lower group velocities above 200 km than the *Hickey and Cole* [1987] profile.

[26] To estimate an upper limit for the time it takes the gravity wave to reach the *F* region peak, we can use the 1.8 h it should take for the wave to reach 200 km and then assume a constant speed of 60 m/s above 200 km up to the *F* region peak, since the *Hines* [1960] profile asymptotically approaches 60 m/s at 200 km. This yields an upper limit on the total time to reach a 400 km *F* region peak of 2.7 h. A lower limit may be estimated for the case where the *F* region peak is at a much lower altitude, say 300 km, and a much higher group velocity due to the inclusion of dissipation. Even for a very high group velocity average speed of 200 m/s above 200 km, we obtain a lower limit estimate of 1.7 h (i.e., 1.6 h + 0.1 h) to reach an *F* region peak at 300 km, using the *Hickey and Cole* [1987] profile.

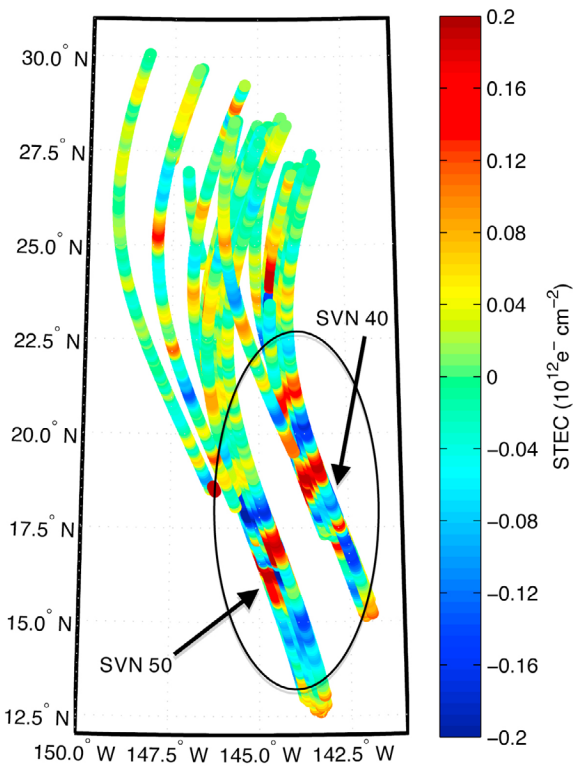

Figure 6. Time convolved variations in TEC observed east of Hawaii following the Samoa Tsunami of 29 September 2009. Data are shown from 23:15 UT, 29 September to 02:00 UT, 30 September. Note the low-high-low variations in the lower right ionospheric pierce point tracks, indicating a traveling ionospheric disturbance that may be associated with the passing ocean tsunami.

[27] Given these estimates of at least 1.7 h for the gravity wave to reach the *F* region peak, the signal observed near the epicenter of the Samoa earthquake was likely not a result of a tsunami-driven gravity wave, since the signal was observed only 10 min after the earthquake occurred. It is more likely that this signal is the result of acoustic waves coming from the earthquake itself, which would likely be present whether or not a tsunami was generated.

[28] The vertical travel time is useful in determining whether a TID could be related to a tsunami in the first few hours after the earthquake and near the epicenter. However, once the gravity wave has reached the ionosphere it should track horizontally with the tsunami below. Therefore, after several hours and far from the epicenter, the vertical travel time is no longer useful in distinguishing between TIDs generated by tsunamis and those produced by other sources. Subsequent observations in this paper occur far afield from the epicenter, so other means are used to identify those perturbations that may be tsunami related.

[29] One way to test the hypothesis that the observed perturbation is caused by an acoustic wave from the earthquake is to plot the variations in TEC in a way that reveals the horizontal velocity of the traveling ionospheric disturbance observed. Figure 5 shows a distance versus time plot of the STEC observations from many GPS receivers in the IGS network within several thousand km of the Samoa earthquake epicenter. Band-pass-filtered STEC values are shown in color as a function of distance between the ionospheric pierce points and the epicenter (ordinate) and Universal Time (UT) (abscissa). This type of distance versus time plot (also known as a "hodochron") is useful because a constant speed can be represented as a straight line, the slope of which is the velocity magnitude. Several constant velocity lines are overplotted on Figure 5; one for Rayleigh wave speed at 3.4 km/s, one for acoustic waves traveling at 1000 m/s, and one for tsunami-driven gravity waves traveling near 200 m/s. There is a strong variation observed within 2000 km of the epicenter, and moving at a horizontal velocity ~1000 m/s, implying that the variations observed near the epicenter were traveling horizontally in the ionosphere at the speed of sound. This seems to indicate that the disturbance seen in Figure 1 was caused by acoustic waves, not gravity waves and is indeed due to the earthquake itself, not the tsunami. Internal gravity waves generated by the tsunami would likely travel horizontally in the atmosphere around the same speed as the tsunami itself, ~200 m/s. No TEC variations aligned near the 200 m/s line are visible near the epicenter.

[30] Variations in TEC observed for this event from receivers on the Hawaiian Islands show wave-like TIDs coincident with the passing of the tsunami as observed in tidal gauges and DART buoys. Figure 6 shows a time-convolved plot of STEC variations at ionospheric pierce point locations in the region a few hundred km east of Hawaii, similar to Figure 3. Note the low-high-low (red-blue-red) variations in multiple ionospheric pierce point tracks in the lower right of Figure 6. These variations are of similar periods (~20 min) to the ocean tsunami periods observed by tidal gauges in Hawaii and are correlated with the MOST model's prediction of where the tsunami wavefront was at that time.

[31] Figure 7 shows this same observation as a distance versus time hodochron plot, similar to Figure 5 but for the region of the ionosphere east of the Hawaiian islands, and only for the two satellites (SVN 40 and 50) shown in Figure 6. Again, the variation is seen between UT 23:30 (September 29) and 00:45 (September 30) as a low-high-low variation with amplitudes up to 0.2 TEC units. The overplotted velocity lines show that these variations are consistent with what we would expect to see from an internal gravity wave traveling with a horizontal wave velocity near 200 m/s coming from the epicenter of the Samoa tsunami. The perturbations are traveling with a horizontal velocity of over 220 m/s, based on the slope of the variations in Figure 7.

[32] While we are convinced this observation is indeed caused by the tsunami, it is important to consider the context in which these observations would be received under a real-time monitoring scenario. If we were using GPS receivers at Hawaii to attempt to observe an inbound tsunami via TEC as it is approaching, we would likely be using all available receivers and satellites to search for the signal. Figure 8 shows a hodochron plot displaying band-pass-filtered TEC observations for all available GPS receivers on the Hawaiian Islands, and all GPS satellites in the receivers' fields of view. The same TID observed so clearly in Figure 7 is still visible in the upper left of Figure 8. While many receivers and two different satellites observe the TID, measurements of band-

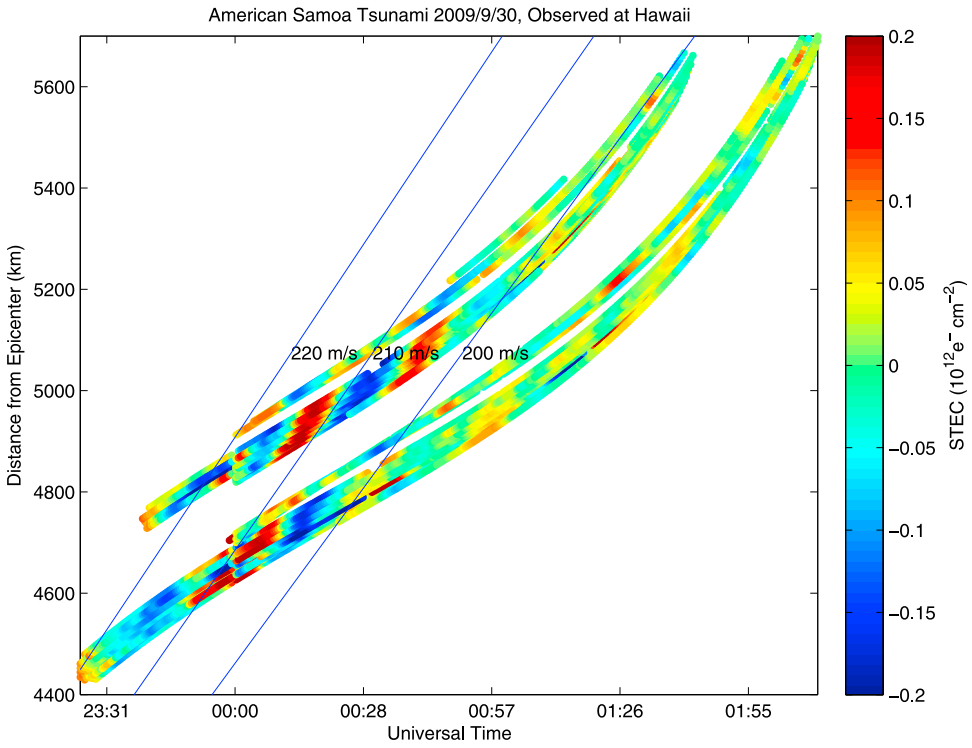

Figure 7. Hodochron plot showing variation in STEC observed by two satellites communicating with 76 GPS receivers on the Hawaiian islands, shown as a function of UT and distance from the epicenter of the tsunamigenic earthquake, near Samoa.

pass-filtered TEC from other satellites do not show the same clear signature. Sorting out the genuine tsunami-driven signals from other variations in STEC by other receivers in the region will be a challenge that must be addressed in future efforts to develop a real-time detection system.

[33] The same data as displayed in Figure 8 can be shown as a series of instantaneous plots of variations in STEC plotted at the geographical locations of the IPPs. Figure 9 shows a geographic map of the region around the Hawaiian Islands with band-pass-filtered STEC plotted from 76 GPS receivers on Hawaii, most on the Big Island. In addition, sea surface height amplitudes generated by the MOST model are overplotted to show the estimated location of the tsunami wavefronts for this event. Note that, just as the MOST model wavefronts are moving past the IPPs in the southeast region of the map, the STEC variation in that region becomes quite pronounced, correlated with the passage of the ocean tsunami itself. These high-low variations are visible both in this sequence of geographic maps, as well as in the upper left part of the hodochron (Figure 8). Animation S1 in the auxiliary material, which includes the map plots of Figure 9 as frames, shows the propagation of the MOST modeled tsunami past the ionospheric pierce points surrounding the Hawaiian islands and offers insight with regard to the ionospheric response to the tsunami-driven atmospheric gravity wave.[1]

[34] As shown by both Animation S1 and Figures 8 and 9, while the observation of the tsunami-driven TID by two GPS satellites and many GPS receivers is well correlated with the timing of the passage of the ocean tsunami, not every set of filtered TEC measurements shows the signature. Notably those IPPs in the region to the south of the Hawaiian Islands do not observe the signature even as the MOST modeled tsunami passes beneath them (see Animation S1). The inconsistency of these observations suggests that the atmospheric gravity wave has a variable degree of impact on the ionospheric electron density and that the geometry of the various TEC raypaths can play an important role in whether the tsunami-driven TID is detectable. While the signature certainly appears to be observable under certain circumstances, challenges remain in developing a future warning system that incorporates this method of tsunami detection.

[35] Interestingly, though tidal gauges along the coast of California show tsunami amplitudes ~10 cm close to shore from this event, no ionospheric TIDs were observed to accompany the ocean tsunami in the ionosphere over California. One possible explanation for this absence of observation may be that the tsunami was too weak to generate a significant internal gravity wave by the time it reached the U.S. west coast. This may be understandable, as the energy of a given section of the tsunami should decrease as the waves expand farther outward from the epicenter. The two DART buoys stationed off California's coast (station 46412, 190 nautical miles (1 nautical mile = 1.852 km) west-southwest of San Diego; and station 46411 stationed 260 nautical miles northwest of San Francisco) detected no significant tsunami, and were not triggered to enter their "event mode" of higher time resolution data logging. The

[1] Auxiliary materials are available in the HTML. doi:10.1029/2010JA016204.

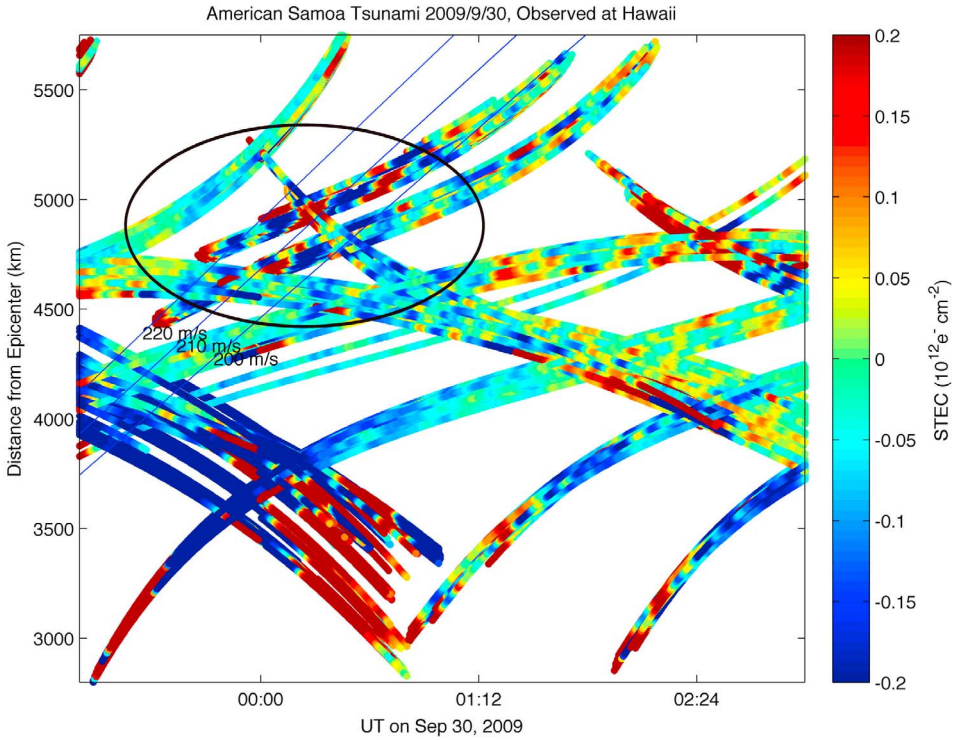

Figure 8. Distance from epicenter versus time plot showing band-pass-filtered STEC for 76 GPS receivers on the Hawaiian Islands at the time the tsunami passed by the islands. Overplotted lines show the expected alignment of variations traveling at internal gravity wave speeds ~200 m/s. Oval highlights tsunami-driven signature.

next closest DART buoys to observe the tsunami, station 46404, 230 nautical miles west of Astoria, Oregon, and station 46407 210 nautical miles west of Cocos Bay, Oregon, detected a sea surface height variation with amplitude <2 cm. This is less than half the amplitude of the tsunami when it was observed near the epicenter at DART stations 51425 (Figure 2) and 51426. All other DART buoys along the west coast of North America and the Aleutian Islands detected sea surface variations of <1 cm. This may suggest a minimum sea surface height threshold for a tsunami that can produce an atmospheric gravity wave observable in ionospheric TEC. A sustainable atmospheric gravity wave is more likely to be generated by larger amplitude sea surface height variations in the deep ocean, rather than the high-amplitude waves occurring for a much shorter period of time as the waves arrive in the nearshore region. Hence it is perhaps understandable that no variation in ionospheric TEC was observed in Southern California for this event.

3.2. Chile Tsunami of 27 February 2010

[36] We also search for tsunami-driven internal gravity waves from the Chile tsunami of 27 February 2010, as the ocean waves were detected in tidal gauges and buoys throughout the Pacific Basin. This tsunami was generated by a magnitude 8.8 earthquake which occurred at 06:34 UT about 115 km northeast of the coastal town of Concepción, Chile. For this event, we analyzed TEC data from GPS receivers in Chile, Hawaii, Southern California, and Japan in order to observe the variation in TEC caused by tsunami-driven internal gravity waves traveling through the ionosphere.

[37] There are few GPS receivers from the IGS network along the South American west coast. We used 6 IGS receivers to investigate the ionospheric behavior in the few hours immediately after the earthquake. Figure 10 shows a hodochron plot for the IPPs within 2000 km of the epicenter of the Chile earthquake. Again, velocity lines are plotted for tsunami-driven internal gravity waves, acoustic waves, and Rayleigh waves. There appear to be traveling ionospheric disturbances with horizontal velocities of ~1000 m/s, and ~3400 m/s (both likely earthquake-generated signatures) but no clear indication of a TID with a horizontal velocity near 200 m/s. There are few IPPs in the region where one would expect to first see a tsunami-driven TID, since the internal gravity wave would take ~2 h to reach the ionosphere, putting the first detection possible at approximately 1500 km away from the epicenter. As such, we look farther afield for a tsunami-driven signature from this event.

[38] Sixty-two GPS receivers on the Hawaiian Islands had data available for TEC observations during the arrival of the tsunami. Figure 11 shows a hodochron plot for STEC data from those receivers, with a 200 m/s horizontal velocity line overplotted. Figure 11 only shows band-pass-filtered STEC variations for TEC raypaths with elevation angles greater than 30°, in order to reduce the amount of low elevation angle data, which tends to have greater noise. There are several clear TIDs that appear to be aligned parallel to the

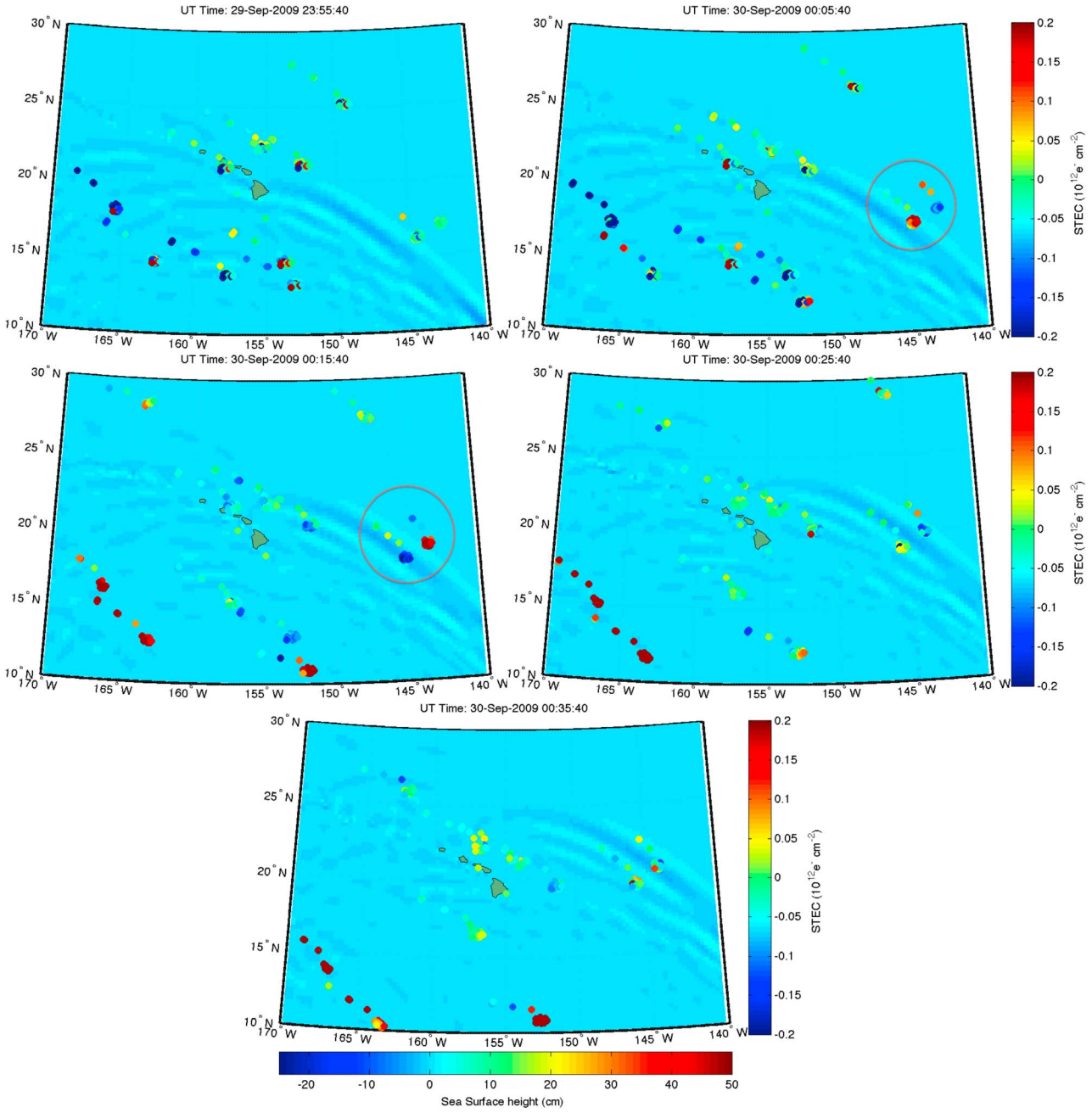

Figure 9. Band-pass-filtered STEC plotted in color at ionospheric pierce point locations for 76 GPS receivers on the Hawaiian Islands and 10 satellites, plotted every 10 min from 22:55:40 UT on 29 September through 00:35:40 UT on 30 September 2009. Tsunami sea surface heights estimated by the MOST model are overplotted to show correlation between variations in STEC and passage of the tsunami. Animation S1 is available in the auxiliary material.

overplotted 200 m/s line. These variations could not be earthquake-generated acoustic waves because any such acoustic waves traveling at a horizontal velocity near 1000 m/s would have long since passed Hawaii by this time. Also, TIDs associated with such acoustic waves would be aligned at a steeper slope corresponding to the 1000 m/s horizontal velocity, the line for which is not shown because it is out of the geographic bounds of Figure 11. Also note that there are several 200 m/s TIDs, each decreasing in intensity and period as time goes on, just as occurs with ocean tsunami waves.

[39] We also processed TEC data from over 350 GPS receivers in the Southern California region for this event. Each of those GPS receivers was in line of sight with up to 12 GPS satellites at one time, resulting in several thousand sets of STEC observations. We applied the *Hickey et al.* [2009] SFWM for this region, using as input the sea sur-

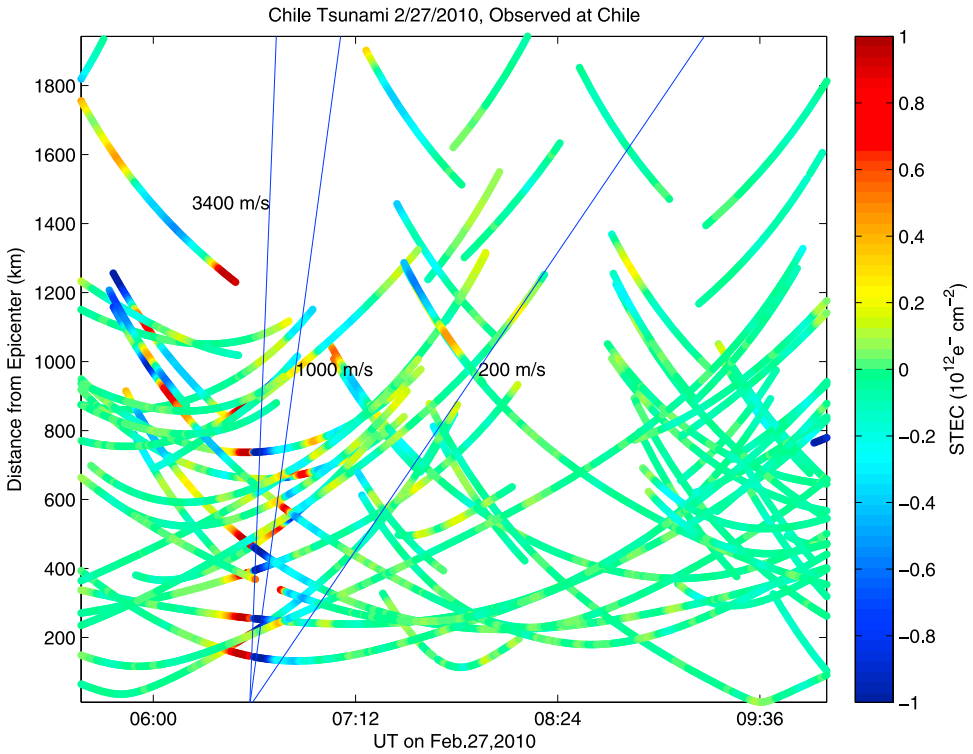

Figure 10. Slant TEC variation (shown in color) at ionospheric pierce points at an altitude of 400 km, plotted as a function of distance from the epicenter of the Chile earthquake of 27 February 2010 and UT. Lines show horizontal velocities of three different types of atmospheric waves: gravity waves (200 m/s), acoustic waves (1000 m/s), and Rayleigh waves (3400 m/s).

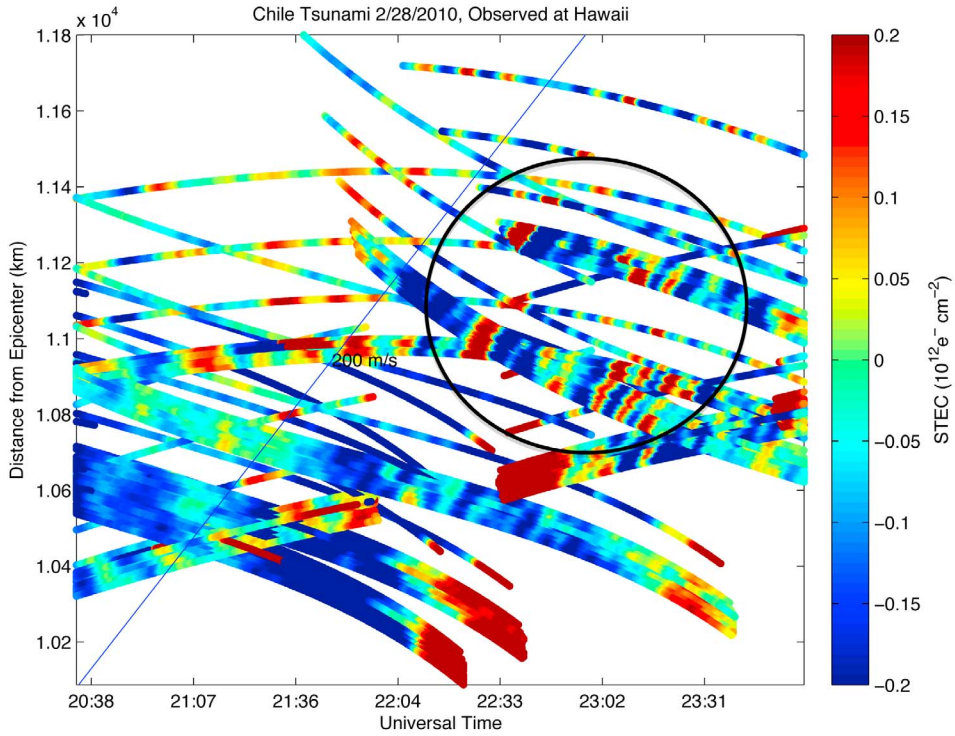

Figure 11. Band-pass-filtered slant TEC variation (shown in color) at ionospheric pierce points at an altitude of 400 km, plotted as a function of distance from the epicenter of the Chile earthquake of February 2010 and UT. Line shows horizontal velocity of atmospheric gravity wave traveling at an average speed of 200 m/s. Oval highlights tsunami-driven TIDs, parallel to the 200 m/s velocity line.

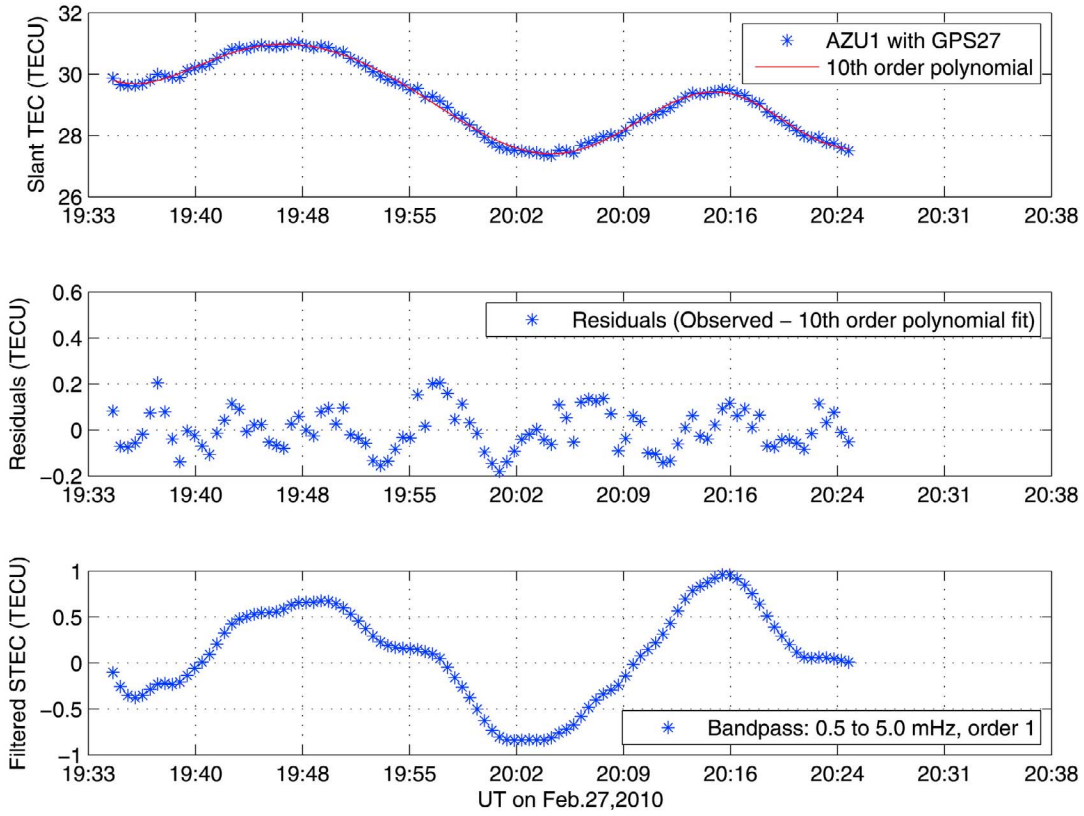

Figure 12. (top) Time series observations of STEC, (middle) residuals with a fit polynomial, and (bottom) band-pass-filtered STEC for the Azusa GPS station in communication with SVN 27 satellite.

face height observations from DART buoy 46412, 190 nautical miles southwest of San Diego, California. At this buoy, the tsunami had amplitude of about 6 cm, with a period of approximately 24 min. The SFWM model predicts an ionospheric TEC variation of 2–2.5% of the background should occur based on this lower boundary input.

[40] Figure 12 shows a time series plot from the Azusa (AZU1) GPS receiver in eastern Los Angeles County, one of the stations in the Plate Boundary Observatory (PBO) array. Figure 12 is similar to Figure 1, with the lone vertical line indicating the time at which the tsunami arrived at the DART buoy several hundred km offshore of San Diego, California. A strong variation in STEC with a period of about 28 min is visible in both the absolute TEC and the band-pass-filtered TEC. (The tenth-order polynomial fits the absolute TEC, including the variation, so it does not show the same variation in the residuals in this case.) The amplitude of the variation is ~0.6–1 TECU, with a background absolute TEC ranging from 27 to 31 TECU. Thus the observed variation has a range of approximately 1.9–3.7% of the background TEC, in acceptable agreement with the model-predicted 2–2.5%, and the period is similar as well (~28 min in TEC versus 24 min in the ocean).

[41] While this observation from an individual receiver may seem to corroborate the model's prediction, when we investigate additional receivers we find that the observed TID is indeed significant, yet it appears to be propagating toward the southeast, while the tsunami is propagating toward the northwest. Figure 13 shows a sequence of geographical maps showing the band-pass-filtered variations in STEC at IPP locations, similar to what is shown in Figure 9 but for the region around California at the time when the Chile tsunami is passing through the region. Again, the MOST model sea surface heights are overplotted to show the location of the tsunami wavefronts at each time-stamped map. There is a significant TID observed by two satellites in Figure 13 (right). The disturbance is visible by most of the GPS receivers, and two of the GPS satellites, so it is likely to be a real TID, and it appears to be propagating toward the southeast. This seems to be an example of a coincidental observation of a TID from another source, unrelated to the passing tsunami. This finding is somewhat surprising, as the SFWM suggests that we should see an ionospheric signature of the tsunami in the region near southern California, and similar conditions produce a clear signature of the tsunami at Hawaii. The maps of Figure 13 are frames from Animation S2, which shows the propagation of the TID toward the southeast in greater clarity.

[42] Japan has over 1200 dual-frequency GPS receivers in its GEONET network, making it an excellent region to search for perturbations in ionospheric TEC. Figure 14 shows a hodochron plot of band-pass-filtered STEC (in color) as a function of distance and time in the ionosphere over Japan at the time when the Chilean tsunami arrived in the region, approximately 24 h after the earthquake occurred. Because GEONET is one of the most dense networks of

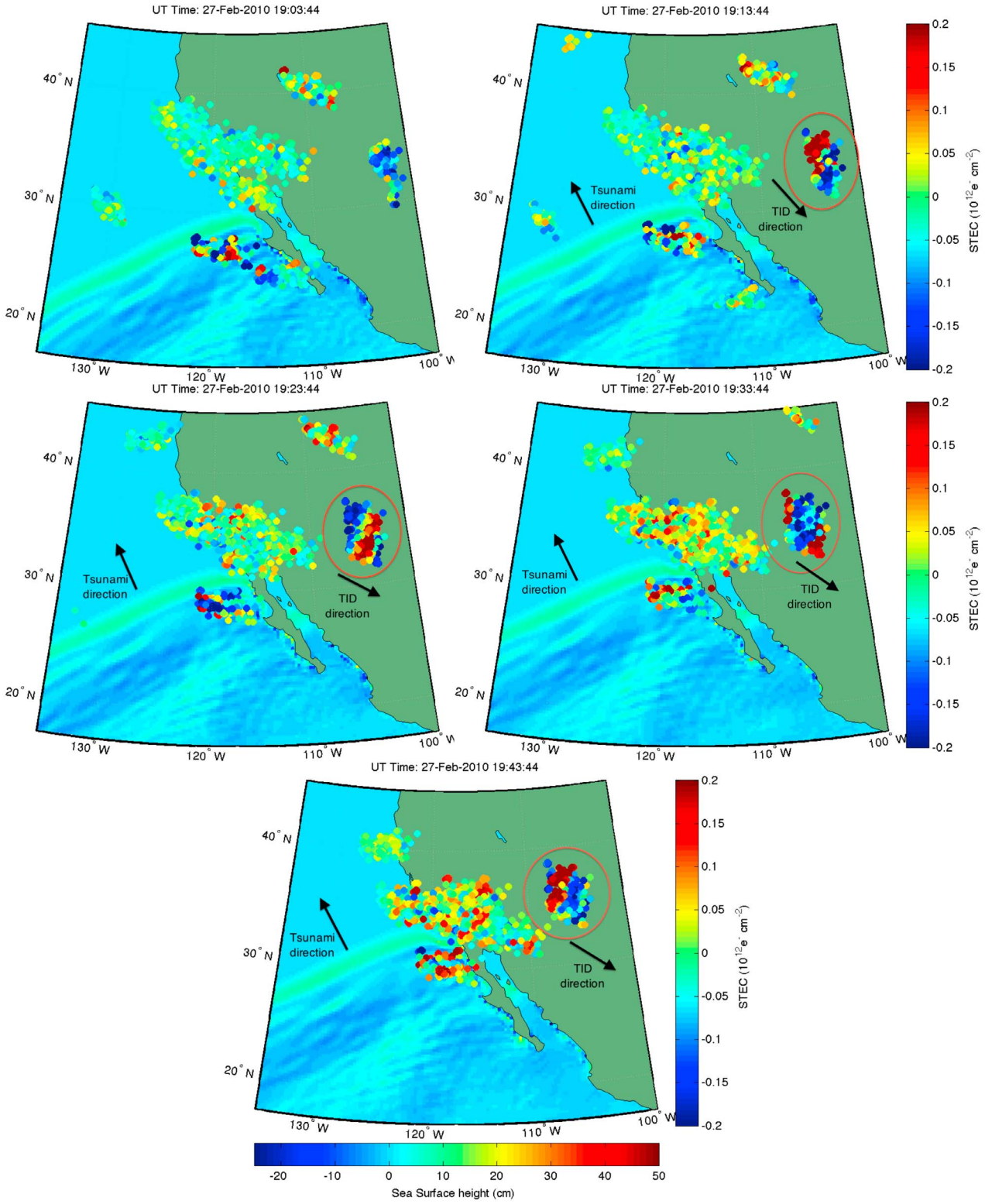

Figure 13. Band-pass-filtered STEC plotted in color at ionospheric pierce point locations for 137 GPS receivers on the U.S. West Coast, plotted every 10 min from 19:03:44 through 19:43:44 on 27 February 2010. Tsunami sea surface heights estimated by the MOST model are overplotted to show correlation between variations in STEC and passage of the tsunami. Circle highlights TID observation. Animation S2 is available in the auxiliary material.

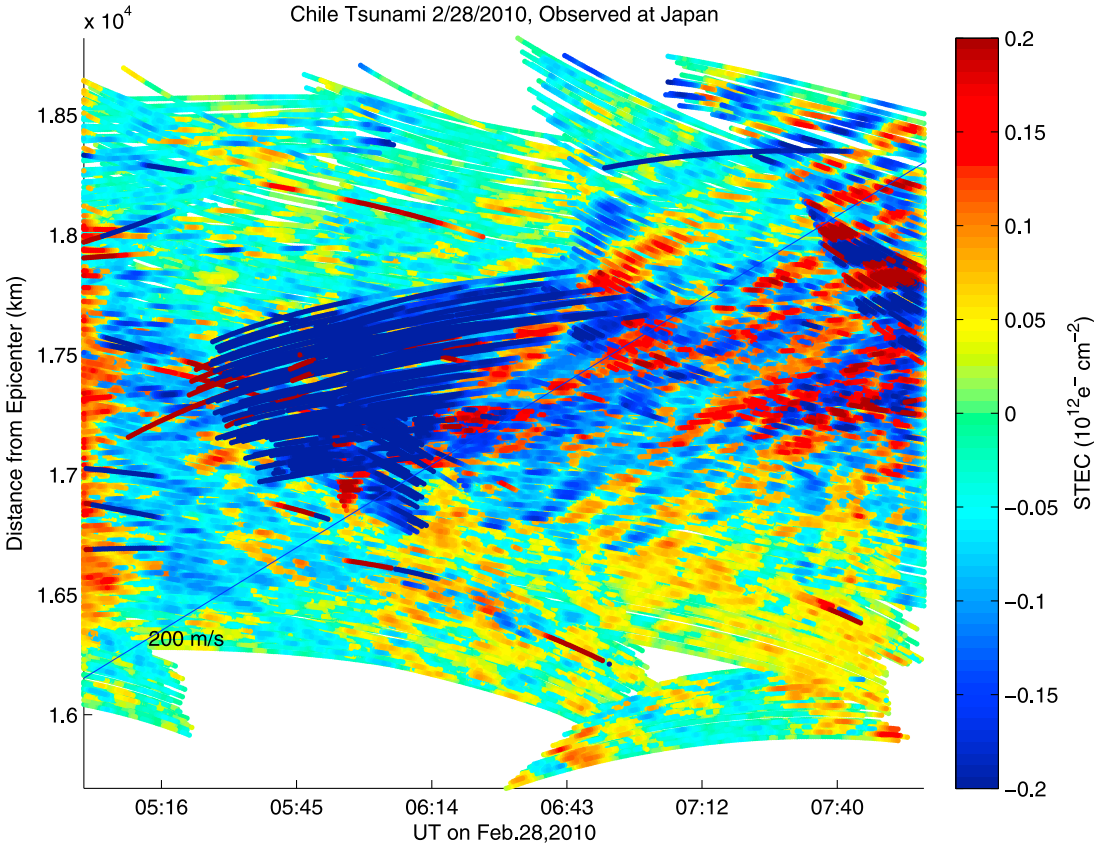

Figure 14. Band-pass-filtered STEC for >200 GPS receivers in Japan following the Chile earthquake. Only data with elevation angle >20° is shown. Overplotted line shows expected alignment of TIDs with an average speed of 200 m/s.

receivers in the world, the data points in the hodochron plot include many different ionospheric measurements at the same time, and in nearly the same location. As a result, some of these measurements will always be "hidden," depending on which measurements are plotted on the top layer of the figure. Figure 14 shows the STEC perturbations plotted in order of absolute value such that those measurements with the largest perturbation are plotted last (on the top layer) and remain visible. The overplotted line shows velocities near the average tsunami speed of ~200 m/s. Although there is a significant amount of noise in the data, there appears to be a signal aligned with the appropriate velocity (ie., a similar slope in the hodochron) for the tsunami (approximately 200 m/s). The TID is visible in STEC observations from multiple satellites and multiple GPS stations in Japan. In fact, there appear to be at least two to three visible waves of perturbed electron density passing over Japan in succession at the time of the tsunami's arrival. The maximum observed perturbation amplitude appears to be approximately 0.1–0.2 TECU. (The swath of dark, off-scale low values visible between 05:20 and 06:45 UT and distances 17,000 and 18,000 km from the epicenter is a data artifact related to the exaggerated TEC values at low elevation angles for one GPS satellite as it comes over the horizon of visibility for the GEONET receivers.)

[43] We performed a spectral full wave model run for the Chile tsunami in the vicinity of Japan, using sea surface height observations from DART buoy 21413, located at 30.515° north latitude, 152.117 east longitude, 690 nautical miles southeast of Tokyo. This model run yielded a maximum expected vertical TEC perturbation of 0.1 TECU, or 0.4% of the mean background TEC. This agrees well with our observation of an approximately 0.1–0.2 TECU amplitude perturbation, shown in Figure 14. Figure 15 shows an approximated ocean tsunami waveform based on the *Peltier and Hines* [1976] analytical expression (dashed curve), with period and wavelength adjusted to the values observed by the 21413 DART buoy. In addition, we plot the ionospheric vertical TEC (solid curve) that we would expect to see as a result of that tsunami waveform, produced on the spectral full wave model. In Figure 16, we overplot that modeled VTEC waveform with an actual VTEC time series from the 0010 GEONET GPS station, which was receiving signals from GPS satellite SVN24. While the modeled VTEC (based on the idealized tsunami waveform from *Peltier and Hines* [1976]) does not match the observed VTEC exactly, the amplitude and period are similar, implying that the spectral full wave model does an acceptable job of approximating the expected ionospheric signature of the ocean tsunami. That is to say: with information (period, wavelength, amplitude) about the ocean surface tsunami observed by the DART buoy, the spectral full wave model was able to produce a time series estimate of the amplitude

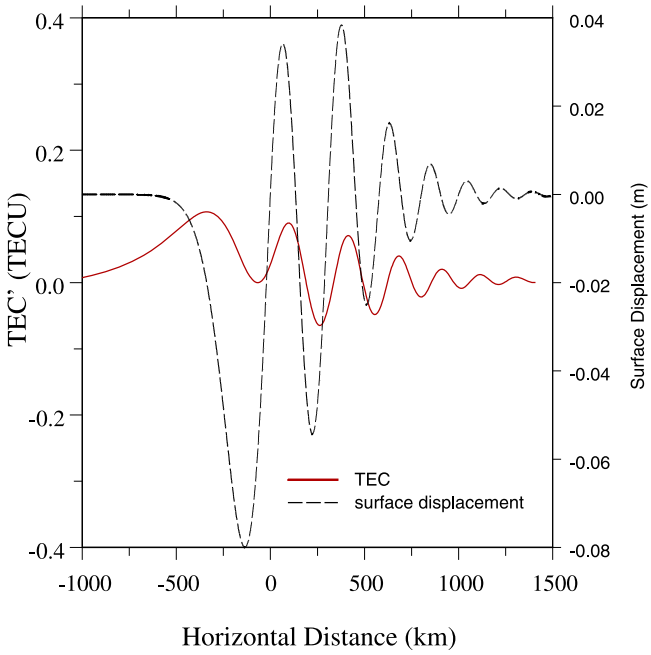

Figure 15. The *Peltier and Hines* [1976] waveform for an idealized tsunami in meters of surface displacement (dashed curve, right axis), modified to have the same period, wavelength, and maximum amplitude as was observed by DART buoy 21413, near Japan, as the Chilean tsunami of 2010 passed by. The solid curve shows the perturbation this idealized tsunami waveform should generate in ionospheric VTEC, as estimated by the spectral full wave model of *Hickey et al.* [2009].

of variation in ionospheric VTEC, which shows reasonable agreement with an observed VTEC signal.

3.3. Elevation Angle Dependence

[44] We are interested in the elevation angle dependence of our band-pass-filtered observations of variation in STEC. Figure 17 shows a plot of band-pass-filtered variations in STEC as a function of elevation angle for Hawaii around the time when the Chilean tsunami was arriving in the region. Note that, in general, lower elevation angles of GPS TEC raypaths correspond, not only to higher absolute STEC values as would be expected, but also to higher amplitude variations in STEC. Similar analyses for other regions show the same elevation angle dependence. This is understandable, since any perturbation in ionospheric electron density would be integrated over a longer raypath for a lower elevation angle than for a higher one. As such, any variations in STEC we observe at lower elevation angles may be exaggerated compared to those at higher elevation angles. This does not mean that variations thought to be associated with tsunamis are not valid if they are observed in STEC at lower elevation angles, but it may mean that the amplitudes of these variations appear artificially amplified in the data. This may be the case in the observation of the tsunami-driven TEC variation presented in Figures 6, 7, and 8, where the variation observed from the initial wavefront of the tsunami arriving at Hawaii (from the Samoa event of 2009) is most visible at IPPs where the elevation angle is less than 20°. Indeed, it would seem that low elevation angle TEC geometry may be a favorable condition for observing tsunami-driven TIDs, due to the enhanced signal in STEC, though any ionospheric noise would be amplified as well.

4. Discussion

[45] To summarize our results, for the Samoa event of 2009, we observed an ionospheric signature of a tsunami-driven internal gravity wave at Hawaii but not near the epicenter or at the U.S. West Coast. The lack of observable signature near the earthquake epicenters is understandable considering the ~2 h it likely takes for the internal gravity wave to reach the *F* region of the ionosphere at 400 km. One might suggest the lack of observation in California after the Samoa event could be explained by very low tsunami wave amplitudes in that region (compared to, for instance, Hawaii) after the tsunami had traversed the entire Pacific Ocean, thus generating an internal gravity wave that is below our TEC detection threshold of 0.01 TECU (precision). However, a tsunami-driven TID was observable in the vicinity of Japan after the Chile event, and Japan is even more distant from the Chile epicenter than California is from the Samoa epicenter. For the Chile event of 2010, we observed what appears to be a tsunami-driven TID at Hawaii and at Japan, far afield from the source, but not near the epicenter and (somewhat surprisingly) not in California. The TEC observations at California deserve further attention in future studies, as we would expect to see a tsunami-driven internal gravity wave there, but instead we observe what appears to be a significant TID moving in the opposite direction, presumably from some source other than the tsunami. Further research is necessary to determine why no tsunami-driven TID was detected in the ionosphere over the California region for these two events.

[46] Note that, in the cases where we did observe a tsunami-driven TID, the amplitude of the signal ranged from 0.1 TECU (Chile event observed at Japan) to >0.2 TECU (Samoa and Chile events observed at Hawaii). Our "background" precision uncertainty in ionospheric TEC measurements is typically 0.1–0.01 TECU [*Mannucci et al.*, 1998, 2004]; therefore, our signal-to-noise ratio ranges from 1 to more than 20, depending on the particular station-satellite combination. Note that, even for the lower signal-to-noise ratios, tsunami-driven signals can be distinguished by determining the direction and speed of propagation. True noise in the ionosphere may be directionless, and TIDs from nontsunami sources may appear but would have directions and horizontal speeds inconsistent with the passing tsunami. The latter was demonstrated in our observations at California following the Chile tsunami of February 2010, in which we observed a TID that was moving in the opposite direction of the tsunami and hence was excluded as a possible signature of the tsunami.

[47] We performed a simulation of atmospheric gravity wave propagation due to the observed tsunami measurements near Hawaii for the Samoa (2009) event and near Japan for the Chile (2010) event. Using the methods of *Hickey et al.* [2009], we took observations of the sea surface height disturbance recorded by the DART buoy 21413 off of Japan and a tidal gauge at Hilo on the big island of Hawaii.

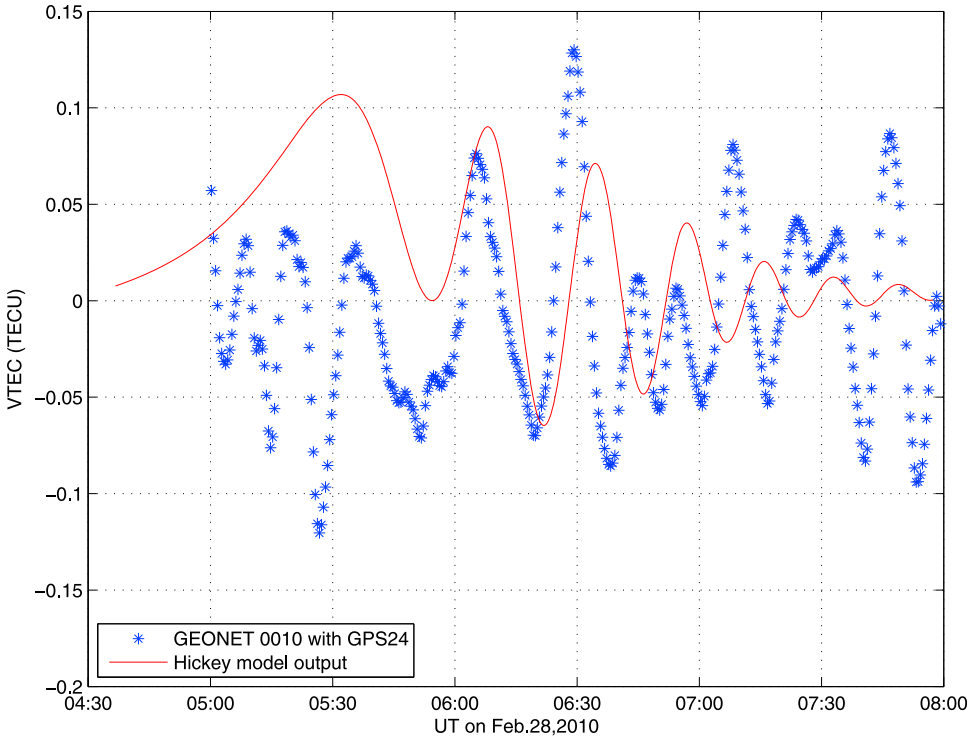

Figure 16. Band-pass-filtered vertical TEC for one satellite-receiver connection (GEONET station 0010 with GPS SVN 24) (dots), overplotted with the modeled VTEC expected from the ocean tsunami properties observed at DART buoy 21413 (solid curve), produced by the spectral full wave model of *Hickey et al.* [2009]. Plotted in TECU as a function of UT.

Using a tidal gauge to approximate deep ocean tsunami characteristics is not ideal due to differences in ocean depth at the nearshore tidal gauge compared to the deep ocean buoy location. However, the DART buoy near Hawaii (station 51407) was not operating when the tsunami was passing through that region, and so DART data are unavailable for Hawaii during the Samoa event. Our simulations suggest that the expected perturbation in vertical TEC over the Hawaiian Islands should be on the order of 1.4% of the background TEC, and the expected perturbation over Japan for the Chile event should be approximately 0.4%. The model results suggest that the proportional perturbation observed at Hawaii from the Samoa tsunami should be 3.5 (i.e., 1.4%/0.4%) times larger than the perturbation at Japan from the Chile tsunami. Comparing with our observations, the maximum amplitude of the perturbation observed at Hawaii from the Samoa event seems to be 0.2 TECU (see Figures 6 and 7), and the average background absolute STEC observed in that region is about 15 TECU, yielding a perturbation percentage of 1.3% (i.e., 0.2/15 = 0.013) The maximum amplitude of the perturbation observed at Japan from the Chile event is approximately 0.1 TECU (see Figure 14), and the average background STEC in that region during the tsunami passage is approximately 20 TECU, yielding a perturbation percentage of 0.5% (i.e., 0.1/20 = 0.005). Hence, the modeled perturbation agrees well with our observation near Hawaii (~1.4% modeled versus 1.3% observed), and near Japan (~0.4% modeled versus 0.5% observed). The observed variations are 0.2/0.1 = 2 times higher at Hawaii than at Japan when comparing the absolute variations in TEC and 1.3/0.5 = 2.6 times higher when comparing variations as a fraction of the background TEC. This observed ratio is similar to what is predicted by the model (a factor of 2.6 versus a factor of 3.5).

[48] Comparing the observations and model results at these two different regions for two different events allows us to point out several different circumstances that contribute to the differences in the observed tsunami-driven TIDs. First, the azimuthal direction of tsunami propagation is quite different in the two cases: the Samoa tsunami arriving at Hilo had an azimuthal direction of 26.73° (clockwise from north), and the Chile tsunami arriving at the DART buoy near Japan had an azimuth of 290.38° (20.38° north of west). These azimuths were estimated by assuming straight propagation along a great circle between the earthquake epicenters and the locations of interest. This means the Samoa tsunami propagation direction was more closely aligned with the Earth's magnetic field at Hawaii than was the Chile tsunami at Japan, and thus we would expect the coupling of the atmospheric gravity wave with the ionosphere to be stronger for the Hawaii observation than for Japan [e.g., *Occhipinti et al.*, 2008; *Hickey et al.*, 2009]. Also, the wave at Hawaii was at a lower latitude, and hence would likely couple more efficiently with the ionosphere due to the geomagnetic field being closer to horizontal at this latitude [*Occhipinti et al.*, 2008]. Finally, the

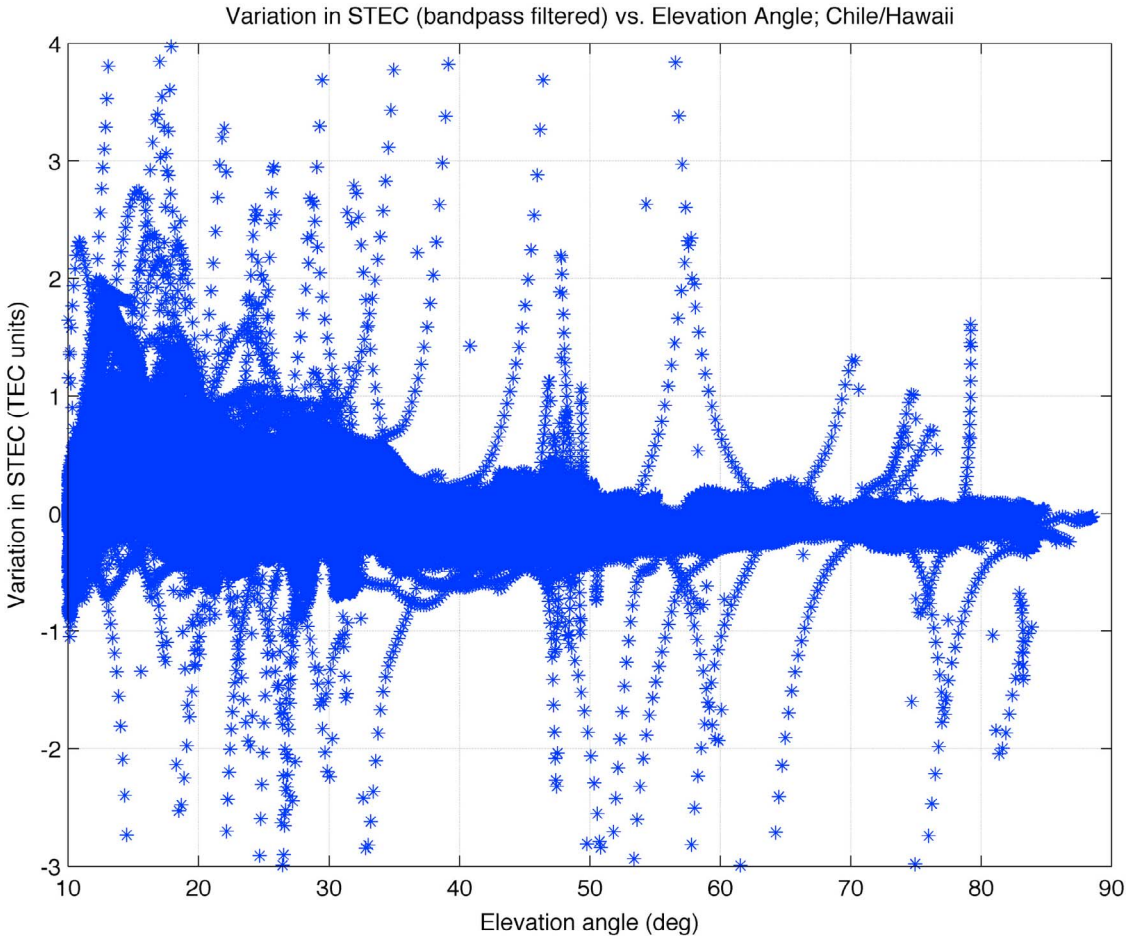

Figure 17. Band-pass-filtered TEC from 62 GPS receivers on the Hawaiian Islands, after the Chile earthquake of 27 February 2010 plotted as a function of elevation angle.

Chilean tsunami waves should be of lower amplitude at Japan due to being much more distant from the earthquake epicenter than the Samoa tsunami arriving at Hawaii.

[49] Due to the geometry involved in TEC raypaths between GPS satellites and ground-based receivers, a disturbance in electron density moving through the ionosphere can be observed from many hundreds of km away (horizontally), allowing the GPS receivers to potentially detect the tsunami-driven TEC variation before the ocean tsunami itself arrives at the shore. Though the ability to make such observations using TEC will vary on a case by case basis, depending on the location of the source epicenter and distribution of GPS receivers and IPPs, this demonstrates that future systems that monitor real-time TEC immediately after a major earthquake could contribute additional early information to an existing tsunami warning system such as that employed by the Pacific Tsunami Warning Center, which currently uses modeled tsunami propagation models (like MOST) and DART buoy and tidal gauge observations.

[50] There are significant challenges remaining in the long term effort to use TEC observations to improve tsunami warning systems. Simply observing TEC variations with amplitudes and periods predicted by an atmosphere-ionosphere coupling model does not prove that a given traveling ionospheric disturbance is associated with a tsunami. Data from multiple receivers in a given region must be analyzed as well to determine the direction and timing of the observed traveling ionospheric disturbance, and whether multiple satellites consistently detect the TEC disturbance. Care must also be taken when analyzing TEC data near the earthquake epicenter, as the earthquake may generate TEC variations that would exist regardless of whether a tsunami was generated or not. This is apparently the case for both the Samoa and Chile events, since we observed acoustic waves (and, in the case of Chile, Rayleigh waves) within about 1500 km of the earthquake epicenter. Also, there are other sources of TIDs, as discussed earlier, and variations can be generated that have similar wave properties to tsunamis without a tsunami being present. However, given the typically known average horizontal propagation velocity of a tsunami (~200 m/s), timing our TEC observations with the expected arrival of the tsunami can help to distinguish those TIDs which are likely to have been caused by the ocean waves, and those TIDs which are unrelated. Tsunami propagation models like MOST are precalculated by NOAA for particular regions and therefore may be available within tens of minutes after a major earthquake (V. Titov, personal communication, 2010). For historical research purposes,

many MOST model results are available at http://nctr.pmel.noaa.gov/database_devel.html. Such models, or even a simple estimate of the average tsunami speed (~200 m/s), can be used to produce a rough estimate of the tsunami arrival time in a particular region. Even narrowing the time window to an uncertainty of several hours over which the tsunami may arrive would be helpful in focusing efforts to observe the tsunami signature in the ionosphere, as it could be used to trigger an algorithm to process high resolution (1 s) TEC data over the period of interest only. Once the time period of interest is determined, the horizontal velocity, period, and propagation direction of any observed TIDs can be used to assess how likely the TID is to be associated with the tsunami. Further research is required to provide an automated routine method of verifying, with many GPS receivers, an observed TEC signal's association with a tsunami.

[51] It is important to note that the TID observed in the ionosphere corresponds to the behavior of the ocean surface tsunami approximately 2 h prior to the observation in TEC. This is due to the fact that the ocean surface perturbation produces an atmospheric gravity wave which takes ~2 h to reach the *F* region peak due to the low vertical propagation velocity. Hence, if the ocean tsunami is altered by arrival at a coast line, the ionospheric TID would likely continue to propagate past the coast for ~2 h after the ocean wave has been stymied, since the last ocean-generated gravity wave would take that long to reach the ionosphere. This phenomenon is apparent in our observations at Japan following the Chile event, in which the observed tsunami-driven TID is actually observed on the leeward side of the islands of Japan. The ionospheric signal has the same direction and speed that the ocean tsunami had before it was blocked by the eastern Japanese coast. Such movement of the tsunami-driven ionospheric TID past the coast of Japan was also observed by *Artru et al.* [2005] for the tsunami caused by the earthquake of 23 June 2001 in Peru.

[52] Based on our results, it seems the best chance to observe TEC variations caused by a tsunami-driven internal gravity wave is to monitor TEC in regions far afield from the epicenter (>1500 km, assuming a vertical propagation velocity of 50 m/s for the internal gravity wave and a horizontal propagation velocity of 200 m/s for the tsunami). Any future augmented tsunami warning systems using the TEC observation technique would therefore be most useful for providing updated observations of tsunami amplitude, period, and velocity parameters used to predict the expected runups at coasts that are distant from the source. The Hawaiian Islands hold a strategic position at the center of the Pacific Ocean, making the dual-frequency GPS receivers there a prime source of TID observations related to tsunamis originating from elsewhere on the Pacific Rim.

[53] Finally, our own results may be compared with those presented by *Rolland et al.* [2010], since that study analyzed tsunami-driven TID signals observed at Hawaii for three different tsunamis, two of which were the Samoa 2009 and Chile 2010 events of our current investigation. *Rolland et al.*'s [2010] study was a discovery-style study, demonstrating that these ionospheric perturbations are indeed associated with tsunamis. In contrast, our present study aims to move past the discovery phase of this phenomenon and evaluate these two particular tsunami events in detail, looking at all available TEC observations, and noting that the tsunami-driven ionosphere signatures are visible in some cases, but not in others. Rolland et al. observed the tsunami-driven TID signatures at Hawaii for both the Samoa 2009 and Chile 2010 events, as we do here, though they presented only the satellite-station connections which show the signal, and not the many other connections in the region which might be expected to observe the signal, but do not. We show these in Figures 8, 9, and 11 (and Figure 14 for the observations at Japan). Our method of surveying all available TEC data in a given region is perhaps more adaptable to what we would observe if we were able to monitor GPS stations in real time during a tsunami. In such a scenario, we would not already know which station-satellite TEC time series would observe the signal and which would not, so we would monitor all available stations, and the challenge would be to quickly pick out the tsunami-driven signal. Furthermore, while Rolland et al. focused solely on Hawaii, a reasonable choice given the island chain's strategic position in the middle of the Pacific Ocean, our study is more exhaustive in geographical scope, looking at the regions near the earthquake epicenters, the U.S. West Coast, and Japan to search for signals.

5. Conclusions

[54] We have found observational evidence of variations in GPS TEC measurements that are associated with the Samoa tsunami of 29 September 2009 and the Chile tsunami of 27 February 2010. Tsunami-driven internal gravity waves are detected as traveling ionospheric disturbances at Hawaii (for the Samoa and Chile events) and at Japan for the Chile event. Future efforts will apply these research techniques to additional tsunami events to further improve our ability to detect and identify tsunami-driven ionospheric disturbances in GPS TEC data. While the scientific questions regarding the nature of this coupling between the ocean and ionosphere are still being studied, our ongoing research efforts should contribute to assessing the logistical issues of developing a TEC monitoring system that takes advantage of existing real-time networks of GPS receivers, such as the NASA Global Differential GPS System (http://www.gdgps.net). Such a system could provide additional information on the inferred amplitude, period, and velocity of a tsunami, based on the observed parameters of the ionospheric internal gravity wave. Such real-time observations could augment the existing tsunami warning system, which currently relies primarily on numerical modeling and buoy observations.

[55] There is also the potential to detect these disturbances by means other than ground-based GPS TEC. Space-based GPS receivers used in radio occultation experiments, as are used on the COSMIC satellite constellation, have been shown to be useful in contributing ionospheric TEC information to improve model-estimated altitude electron density profiles [*Komjathy et al.*, 2010]. It remains to be seen whether COSMIC observations may be useful for variations in electron density over a limited particular geographic region, given the geometry of estimating TEC along the radio signal raypath from the LEO satellite, through the ionosphere, and back out to space to a GPS satellite. In addition, recent modeling work by *Hickey et al.* [2010] suggests that tsunami-driven ionospheric gravity waves should be visible as variations in thermospheric nightglow, citing potential

brightness fluctuations of 50% and 43% in the OI 6300 Å and O 1356 Å emissions. Both techniques show some initial promise and should be pursued in the future.

[56] **Acknowledgments.** The authors would like to thank John LaBrecque of NASA Headquarters and the Earth Science and Interior NASA ROSES grant (NNH07ZDA001N-ESI), which made this research possible. James Foster of the University of Hawaii provided access to RINEX files from additional GPS receivers on the Big Island of Hawaii. RINEX files from over 1200 GPS receivers in the Japanese GPS Earth Observation (GEONET) network were provided by the Geospatial Information Authority (GSI), a part of the Japanese Ministry of Land, Infrastructure, Transport and Tourism. Edison Gica, Yong Wei, and Vasily Titov of the NOAA Center for Tsunami Research provided access to the MOST model results for the Samoa (2009) and Chile (2010) tsunami events. Their excellent overview results from these and other tsunami events are available at http://nctr.pmel.noaa.gov/database_devel.html. Phillip Stephens in the Ionospheric and Atmospheric Remote Sensing group at JPL also provided useful suggestions and commentary during this research analysis. Data analysis was performed at the Jet Propulsion Laboratory, California Institute of Technology, under contract to the National Aeronautics and Space Administration. Modeling work was performed at Embry Riddle Aeronautical University.

[57] Robert Lysak thanks the reviewers for their assistance in evaluating this paper.

References

Artru, J., P. Lognonné, and E. Blanc (2001), Normal modes modelling of post-seismic ionospheric oscillations, *Geophys. Res. Lett.*, *28*, 697–700, doi:10.1029/2000GL000085.

Artru, J., V. Ducic, H. Kanamori, P. Lognonné, and M. Murakami (2005), Ionospheric detection of gravity waves induced by tsunamis, *Geophys. J. Int.*, *160*, 840–848, doi:10.1111/j.1365-246X.2005.02552.x.

Basu, S., K. M. Groves, J. M. Quinn, and P. Doherty (1999), A comparison of TEC fluctuations and scintillations at Ascension Island, *J. Atmos. Sol. Terr. Phys.*, *61*, 1219–1226, doi:10.1016/S1364-6826(99)00052-8.

Bust, G. S., and C. N. Mitchell (2008), History, current state, and future directions of ionospheric imaging, *Rev. Geophys.*, *46*, RG1003, doi:10.1029/2006RG000212.

Calais, E., and J. B. Minster (1995), GPS detection of ionospheric perturbations following the January 17, 1994, Northridge earthquake, *Geophys. Res. Lett.*, *22*, 1045–1048, doi:10.1029/95GL00168.

Cosgrave, J. (2007), Synthesis report: Expanded summary, joint evaluation of the international response to the Indian Ocean tsunami, 42 pp., Tsunami Eval. Coalition, London. (Available at http://www.alnap.org/pool/files/Syn_Report_Sum.pdf.)

Daniels, F. B. (1952), Acoustical energy generated by the ocean waves, *J. Acoust. Soc. Am.*, *24*, 83, doi:10.1121/1.1906855.

Hajj, G., R. Ibanez-Meier, and E. Kursinski (1994), Imaging the ionosphere with the global positioning system, *Int. J. Imaging Syst. Technol.*, *5*, 174–187, doi:10.1002/ima.1850050214.

Hickey, M. P., and K. D. Cole (1987), A quartic dispersion equation for internal gravity waves in the thermosphere, *J. Atmos. Terr. Phys.*, *49*, 889–899, doi:10.1016/0021-9169(87)90003-1.

Hickey, M. P., G. Schubert, and R. L. Walterscheid (2009), Propagation of tsunami-driven gravity waves into the thermosphere and ionosphere, *J. Geophys. Res.*, *114*, A08304, doi:10.1029/2009JA014105.

Hickey, M. P., G. Schubert, and R. L. Walterscheid (2010), Atmospheric airglow fluctuations due to a tsunami-driven gravity wave disturbance, *J. Geophys. Res.*, *115*, A06308, doi:10.1029/2009JA014977.

Hines, C. O. (1960), Internal atmospheric gravity waves at ionospheric heights, *Can. J. Phys.*, *38*, 1441, doi:10.1139/p60-150.

Hines, C. O. (1972), Gravity waves in the atmosphere, *Nature*, *239*, 73–78, doi:10.1038/239073a0.

Hines, C. O., et al. (1974), *The Upper Atmosphere in Motion*, *Geophysical Monograph Series*, vol. 18, AGU, Washington, D.C.

Hung, R. J., T. Phan, and R. E. Smith (1978), Observation of gravity waves during the extreme tornado outbreak of 3 April 1974, *J. Atmos. Terr. Phys.*, *40*, 831–843, doi:10.1016/0021-9169(78)90033-8.

Kelley, M. C. (1997), In situ ionospheric observations of severe weather-related gravity waves and associated small-scale plasma structure, *J. Geophys. Res.*, *102*, 329–335, doi:10.1029/96JA03033.

Kelley, M. C. (2009), *The Earth's Ionosphere: Plasma Physics and Electrodynamics*, *Int. Geophys. Ser.*, vol. 96, Elsevier Acad., New York.

Kelley, M. C., R. Livingston, and M. McCready (1985), Large amplitude thermospheric oscillations induced by an earthquake, *Geophys. Res. Lett.*, *12*, 577–580, doi:10.1029/GL012i009p00577.

Komjathy, A., L. Sparks, B. D. Wilson, and A. J. Mannucci (2005), Automated daily processing of more than 1000 ground-based GPS receivers for studying intense ionospheric storms, *Radio Sci.*, *40*, RS6006, doi:10.1029/2005RS003279.

Komjathy, A., B. Wilson, X. Pi, V. Akopian, M. Dumett, B. Iijima, O. Verkhoglyadova, and A. J. Mannucci (2010), JPL/USC GAIM: On the impact of using COSMIC and ground-based GPS measurements to estimate ionospheric parameters, *J. Geophys. Res.*, *115*, A02307, doi:10.1029/2009JA014420.

Langley, R. B. (1996), Propagation of the GPS signals, *Lect. Notes Earth Sci.*, *60*, 141, doi:10.1007/BFb0117681.

Lee, M. C., R. Pradipta, W. J. Burke, A. Labno, L. M. Burton, J. A. Cohen, S. E. Dorfman, A. J. Coster, M. P. Sulzer, and S. P. Kuo (2008), Did tsunami-launched gravity waves trigger ionospheric turbulence over Arecibo?, *J. Geophys. Res.*, *113*, A01302, doi:10.1029/2007JA012615.

Mai, C.-L., and J.-F. Kiang (2009), Modeling of ionospheric perturbation by 2004 Sumatra tsunami, *Radio Sci.*, *44*, RS3011, doi:10.1029/2008RS004060.

Mannucci, A. J., B. D. Wilson, D. N. Yuan, C. H. Ho, U. J. Lindqwister, and T. F. Runge (1998), A global mapping technique for GPS-derived ionospheric total electron content measurements, *Radio Sci.*, *33*, 565–582, doi:10.1029/97RS02707.

Mannucci, A. J., et al. (2004), GPS-based remote sensing of the geospace environment: Horizontal and vertical structure of the ionosphere and plasmasphere, *Proc. SPIE Int. Soc. Opt. Eng.*, *5660*, 1–13, doi:10.1117/12.580048.

Meinig, C., S. E. Stalin, A. I. Nakamura, F. González, and H. G. Milburn (2005), Technology developments in real-time tsunami measuring, monitoring and forecasting, paper presented at Oceans 2005, Mar. Technol. Soc., Washington, D. C., 19–23 Sept. (Available at http://nctr.pmel.noaa.gov/Dart/Pdf/mein2836_final.pdf)

Nicolls, M. J., M. C. Kelley, A. J. Coster, S. A. González, and J. J. Makela (2004), Imaging the structure of a large-scale TID using ISR and TEC data, *Geophys. Res. Lett.*, *31*, L09812, doi:10.1029/2004GL019797.

Occhipinti, G., P. Lognonné, E. A. Kherani, and H. Hébert (2006), Three-dimensional waveform modeling of ionospheric signature induced by the 2004 Sumatra tsunami, *Geophys. Res. Lett.*, *33*, L20104, doi:10.1029/2006GL026865.

Occhipinti, G., E. A. Kherani, and P. Lognonné (2008), Geomagnetic dependence of ionospheric disturbances induced by tsunamigenic internal gravity waves, *Geophys. J. Int.*, *173*, 753–765, doi:10.1111/j.1365-246X.2008.03760.x.

Peltier, W. R., and C. O. Hines (1976), On the possible detection of tsunamis by a monitoring of the ionosphere, *J. Geophys. Res.*, *81*, 1995–2000, doi:10.1029/JC081i012p01995.

Richmond, A. D., and S. Matsushita (1975), Thermospheric response to a magnetic substorm, *J. Geophys. Res.*, *80*, 2839–2850, doi:10.1029/JA080i019p02839.

Rolland, L. M., G. Occhipinti, P. Lognonné, and A. Loevenbruck (2010), Ionospheric gravity waves detected offshore Hawaii after tsunamis, *Geophys. Res. Lett.*, *37*, L17101, doi:10.1029/2010GL044479.

Skone, S. (2009), Using GPS TEC measurements to detect geomagnetic Pc 3 pulsations, *Radio Sci.*, *44*, RS0A27, doi:10.1029/2008RS004106.

Tang, A., et al. (2010), Learning from earthquakes: The Mw 8.8 Chile earthquake of 27 February 2010, report, Earthquake Eng. Res. Inst., Oakland, Calif. (Available at http://www.eeri.org/site/images/eeri_newsletter/2010_pdf/Chile10_insert.pdf)

Titov, V. V., and F. I. Gonzalez (1997), Implementation and testing of the Method of Splitting Tsunami (MOST) model, *NOAA Tech. Memo., ERL PMEL-112*, 11 pp. (Available at http://www.pmel.noaa.gov/pubs/PDF/tito1927/tito1927.pdf)

Titov, V. V., and C. E. Synolakis (1997), Extreme inundation flows during the Hokkaido-Nansei-Oki tsunami, *Geophys. Res. Lett.*, *24*(11), 1315–1318, doi:10.1029/97GL01128.

Titov, V. V., A. B. Rabinovich, H. O. Mofjeld, R. E. Thomson, and F. I. González (2005), The global reach of the 26 December 2004 Sumatra tsunami, *Science*, doi:10.1126/science.1114576.

Tsugawa, T., Y. Otsuka, A. J. Coster, and A. Saito (2007), Medium-scale traveling ionospheric disturbances detected with dense and wide TEC maps over North America, *Geophys. Res. Lett.*, *34*, L22101, doi:10.1029/2007GL031663.

Xiao, Z., S. Xiao, Y. Hao, and D. Zhang (2007), Morphological features of ionospheric response to typhoon, *J. Geophys. Res.*, *112*, A04304, doi:10.1029/2006JA011671.

Yeh, K. C., and C. H. Liu (1974), Acoustic-gravity waves in the upper atmosphere, *Rev. Geophys.*, *12*(2), 193–216, doi:10.1029/RG012i002p00193.

Yizengaw, E., H. Wei, M. B. Moldwin, D. Galvan, L. Mandrake, A. Mannucci, and X. Pi (2005), The correlation between mid-latitude trough and the plasmapause, *Geophys. Res. Lett.*, *32*, L10102, doi:10.1029/2005GL022954.

D. A. Galvan, A. Komjathy, and A. J. Mannucci, Ionospheric and Atmospheric Remote Sensing Group, Jet Propulsion Laboratory, California Institute of Technology, 4800 Oak Grove Dr., Pasadena, CA 91109, USA. (david.galvan@jpl.nasa.gov)

M. P. Hickey, Department of Physical Sciences, Embry Riddle Aeronautical University, 600 S. Clyde-Morris Blvd., Daytona Beach, FL 32114, USA.